Caveolae in CNS arterioles mediate neurovascular coupling

https://doi.org/10.1038/s41586-020-2026-1

Received: 19 February 2019

Accepted: 3 January 2020

Published online: 19 February 2020

Check for updates

Brian W. Chow[1,3], Vicente Nuñez[1,3], Luke Kaplan[1], Adam J. Granger[1,2], Karina Bistrong[1], Hannah L. Zucker[1], Payal Kumar[1], Bernardo L. Sabatini[1,2] & Chenghua Gu[1]✉

Proper brain function depends on neurovascular coupling: neural activity rapidly increases local blood flow to meet moment-to-moment changes in regional brain energy demand[1]. Neurovascular coupling is the basis for functional brain imaging[2], and impaired neurovascular coupling is implicated in neurodegeneration[1]. The underlying molecular and cellular mechanisms of neurovascular coupling remain poorly understood. The conventional view is that neurons or astrocytes release vasodilatory factors that act directly on smooth muscle cells (SMCs) to induce arterial dilation and increase local blood flow[1]. Here, using two-photon microscopy to image neural activity and vascular dynamics simultaneously in the barrel cortex of awake mice under whisker stimulation, we found that arteriolar endothelial cells (aECs) have an active role in mediating neurovascular coupling. We found that aECs, unlike other vascular segments of endothelial cells in the central nervous system, have abundant caveolae. Acute genetic perturbations that eliminated caveolae in aECs, but not in neighbouring SMCs, impaired neurovascular coupling. Notably, caveolae function in aECs is independent of the endothelial NO synthase (eNOS)-mediated NO pathway. Ablation of both caveolae and eNOS completely abolished neurovascular coupling, whereas the single mutants exhibited partial impairment, revealing that the caveolae-mediated pathway in aECs is a major contributor to neurovascular coupling. Our findings indicate that vasodilation is largely mediated by endothelial cells that actively relay signals from the central nervous system to SMCs via a caveolae-dependent pathway.

Despite representing only 2% of body mass, the brain uses 20% of the body's energy at rest and has very limited ability to store energy[3]. To meet acute changes in regional brain energy demand, a process called neurovascular coupling rapidly increases local blood flow following neural activation[1]; this is also the basis for functional brain imaging, one of the few techniques currently available to image and measure activity in the human brain in both health and disease[2].

Neurovascular coupling begins with increased neural activity and ends with SMC relaxation leading to arteriolar vasodilation and increased capillary blood flow[2,4]. This process occurs rapidly, on the order of hundreds of milliseconds in vivo under physiological conditions[5–7]. How signals are transmitted from neurons to SMCs is not completely understood. The conventional view has been that following neural activity, neurons and astrocytes release vasodilatory signals that act directly on SMCs to relax and expand arteriolar diameter to increase blood flow[1]. However, recent studies have indicated that blood vessels can also sense changes in neural activity[6,8,9], but the mechanisms underlying how these endothelial cells (ECs) in the central nervous system (CNS) mediate neurovascular coupling remains largely unknown.

Here, we demonstrate that CNS aECs actively mediate signals from neurons to facilitate the relaxation of SMCs during neurovascular coupling. We found that unlike other segments of ECs in the CNS vasculature, aECs contain abundant caveolae. We used in vivo two-photon microscopy for simultaneous measurement of neural activity and vascular dynamics (arteriolar vessel diameter and capillary blood flow) in the barrel cortex of awake mice following whisker stimulation. Acute genetic perturbations that eliminated caveolae in aECs, but not in neighbouring SMCs, impaired neurovascular coupling. Moreover, caveolae function in aECs is independent of the eNOS-mediated NO pathway, and ablation of both caveolae and eNOS completely abolished neurovascular coupling, revealing that the caveolae-mediated pathway in aECs is a major contributor to neurovascular coupling. Finally, we demonstrate that MFSD2A, a molecular suppressor of caveolae formation, is absent in aECs and that ectopic expression of MFSD2A specifically in aECs is sufficient to impair neurovascular coupling. Our findings indicate that ECs actively mediate signals from neurons and astrocytes to SMCs via a caveolae-dependent pathway, which is a major mechanism underlying neurovascular coupling.

CNS arteriolar ECs have abundant caveolae

It has previously been shown that caveolae are actively suppressed in most CNS ECs to ensure blood–brain barrier integrity[10–12]. However, this suppression of caveolae is not uniform in all segments of the CNS endothelium as aECs have abundant caveolae (Fig. 1b, d), in contrast to negligible numbers of caveolae in capillary ECs (cECs) (Fig. 1a, d).

[1]Department of Neurobiology, Harvard Medical School, Boston, MA, USA. [2]Howard Hughes Medical Institute, Department of Neurobiology, Harvard Medical School, Boston, MA, USA. [3]These authors contributed equally: Brian W. Chow, Vicente Nuñez. ✉e-mail: chenghua_gu@hms.harvard.edu

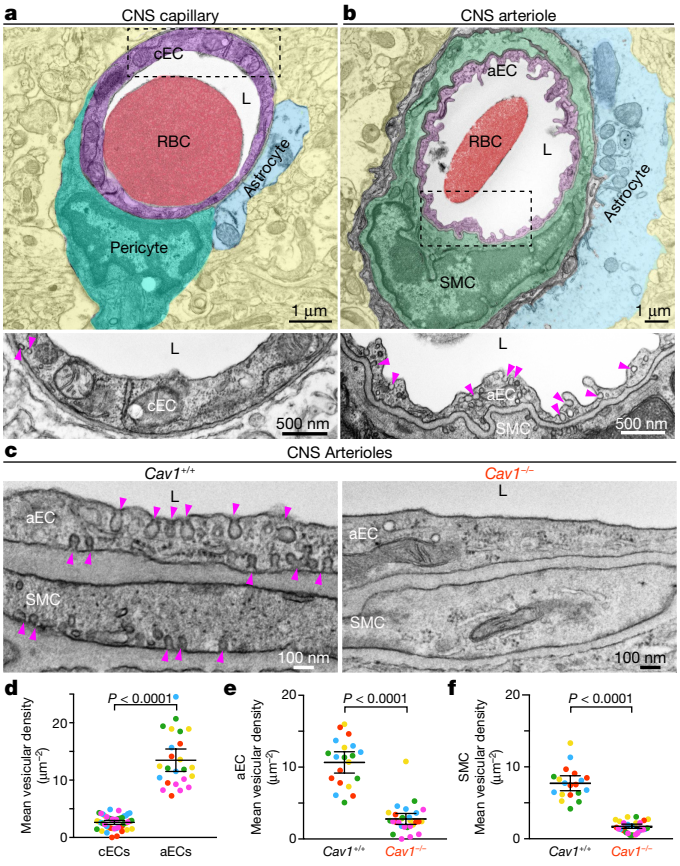

Fig. 1 | CNS arterioles have abundant caveolae. a, Transmission electron microscopy image of a CNS capillary. Pseudocolours highlight different cells: cEC (purple), pericyte (teal), astrocyte end-foot (blue), red blood cell (RBC, red), lumen (L) (white) and neuropil (yellow). Bottom shows an inverted, magnified image of the boxed area in the top panel. **b**, Transmission electron microscopy image of a CNS arteriole. Pseudocolours highlight different cells: aEC (purple), SMC (green), astrocyte end-foot (blue) and neuropil (yellow). Bottom shows a magnified image of the boxed area in the top panel. Arrowheads point to vesicles (**a**, **b**). **c**, Transmission electron microscopy images of aECs and SMCs from *Cav1*$^{+/+}$ and *Cav1*$^{-/-}$ mice. Arrowheads point to caveolae. **d**, Mean vesicular density in cECs and aECs from wild-type mice ($n = 5$ mice, 46 capillaries and 24 arterioles). **e**, **f**, Mean vesicular density in aECs (**e**) and SMCs (**f**) in *Cav1*$^{+/+}$ ($n = 5$ mice, 20 arterioles) and *Cav1*$^{-/-}$ mice ($n = 5$ mice, 28 arterioles). Data are mean ± s.e.m.; nested, unpaired, two-tailed *t*-test (**d**–**f**).

cECs and aECs can be distinguished under transmission election microscopy: capillaries have a smooth lumen whereas arterioles have a ruffled lumen; cECs are also surrounded by pericytes, whereas aECs are sheathed by SMCs (Fig. 1a, b). The abundant vesicles in aECs are abolished in *caveolin-1*-mutant (*Cav1*$^{-/-}$) mice, suggesting that they are composed of caveolae (Fig. 1c, e). Caveolin 1 is an essential component of caveolae and the endothelium of *Cav1*$^{-/-}$ mice lacks caveolae[11–14]. Thus, CNS aECs have abundant caveolae, consistent with a previous study[15]. Notably, many caveolae are also present in the SMCs that wrap around the aECs (Fig. 1c, f).

Neurovascular coupling requires caveolae

Because caveolae are specifically abundant in aECs, and CNS arterioles are the site of vasodilation[2,4], we examined *Cav1*$^{-/-}$ mice to determine whether caveolae are important for neurovascular coupling. To study neurovascular coupling in vivo, we optimized a two-photon microscope for simultaneous measurement of neural activity and vascular dynamics, including arteriolar vessel diameter and capillary blood flow at single-vessel resolution in awake mice (Extended Data Fig. 1).

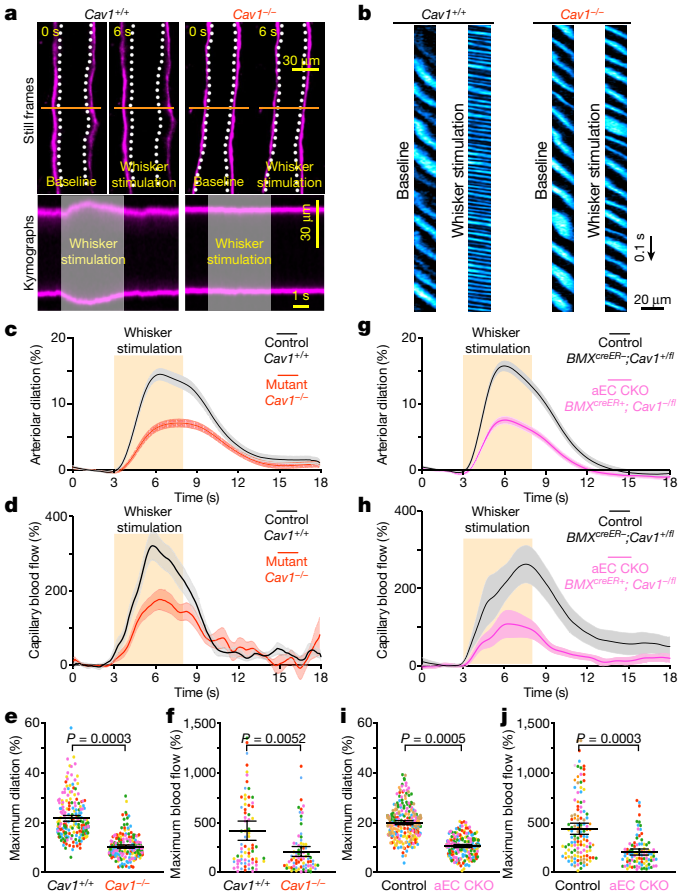

Fig. 2 | Caveolae in CNS aECs specifically are required for neurovascular coupling. a, Still frame images of pial arteries during neurovascular coupling in *Cav1*$^{+/+}$ and *Cav*$^{-/-}$ mice using in vivo two-photon microscopy. Top, Hydrazide-stained arterioles during baseline and whisker stimulation. White hashes outline the arterioles during baseline period. Bottom, kymographs of the arteriolar dilation, generated by transverse line scans (orange lines in top images). The grey rectangle in the kymograph represents the whisker stimulation period. **b**, Kymographs of red blood cell flow in capillaries for *Cav1*$^{+/+}$ and *Cav1*$^{-/-}$ mice. Dark streaks represent red blood cells, blue streaks represent the fluorescent tracer-filled capillary lumen. Left and right kymographs show red blood cell flow during baseline and whisker stimulation, respectively. **c**–**f**, Time course of change in arteriolar dilation (**c**), change in red blood cell velocity (**d**), maximum change in arteriolar dilation (**e**) and maximum red blood cell velocity (**f**) in *Cav1*$^{+/+}$ ($n = 5$ mice, 196 arterioles, 77 capillaries) and *Cav1*$^{-/-}$ mice ($n = 5$ mice, 194 arterioles, 79 capillaries). **g**–**j**, Time course of change in arteriolar dilation (**g**), change in red blood cell velocity (**h**), maximum change in arteriolar dilation (**i**) and maximum red blood cell velocity (**j**) in control (*BMX*$^{creER-}$;*Cav1*$^{+/fl}$; $n = 7$ mice, 260 arterioles, 122 capillaries) and aEC conditional *Cav1*-knockout mice (*BMX*$^{creER+}$;*Cav1*$^{-/fl}$; $n = 5$ mice, 193 arterioles, 94 capillaries). Data are mean ± s.e.m.; nested, unpaired, two-tailed *t*-test (**e**, **f**, **i**, **j**).

We focused on the barrel cortex, a well-characterized region of mouse somatosensory cortex that processes sensory input from the vibrissae[16]. Sensory stimulation by whisker brushing in awake mice evoked spatially and temporally patterned neural activity that can be imaged in the barrel cortex by intracellular calcium levels in mice expressing the calcium sensor GCaMP6s in neurons (*Thy1*-GCaMP6s) (Extended Data Fig. 1b, c). Hydrazide[5] and quantum dots were injected intravenously into *Thy1*-GCaMP6s mice to visualize arterioles and image capillary blood flow, respectively. Upon whisker brushing, we observed a robust increase in the GCaMP signal in neurons, followed by arteriolar dilation and increased red blood cell velocity (measured by tracking the movement of red blood cells, which are devoid of quantum dots and thus appear dark) (Extended Data Fig. 1b–g, Supplementary Videos 1–3).

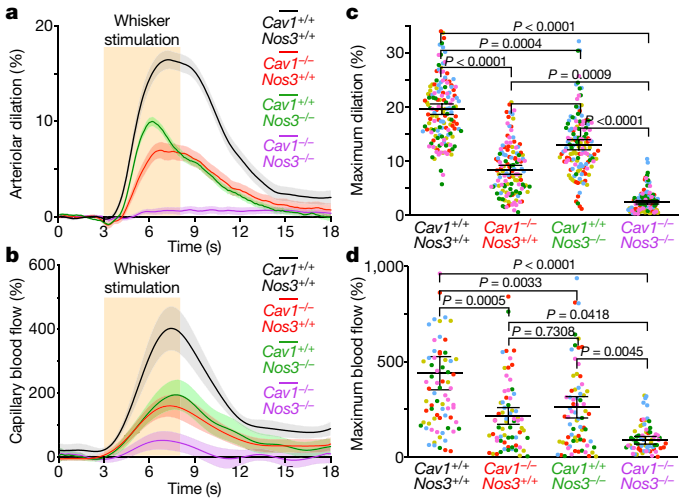

Fig. 3 | Caveolae in aECs mediate neurovascular coupling independently of eNOS. Time course of change in arteriolar dilation (**a**), change in red blood cell velocity (**b**), maximum percentage change in arteriolar dilation (**c**) and maximum percentage change in red blood cell velocity (**d**) in *Cav1*$^{+/+}$*Nos3*$^{+/+}$ ($n = 5$ mice, 148 arterioles, 76 capillaries), *Cav1*$^{-/-}$*Nos3*$^{+/+}$ ($n = 5$ mice, 128 arterioles, 68 capillaries), *Cav1*$^{+/+}$*Nos3*$^{-/-}$ ($n = 5$ mice, 137 arterioles, 73 capillaries) and *Cav1*$^{-/-}$*Nos3*$^{-/-}$ mice ($n = 5$ mice, 139 arterioles, 74 capillaries). Data are mean ± s.e.m.; nested, one-way analysis of variance (ANOVA) with a post hoc Bonferroni multiple comparison adjustment (**c**, **d**).

Finally, in contrast to the robust vasodilation observed in the barrel cortex (using our in vivo whisker stimulation paradigm), the retrosplenial cortex—a brain region not associated with processing whisking[17]—exhibits very low levels of vasodilation (Extended Data Fig. 1h, i). This result indicates that the changes in arterial vessel diameter are a result of the whisker-stimulus-dependent neural activity and not systemic variables.

Cav1$^{-/-}$ mice exhibited attenuated arteriolar dilation upon whisker stimulation, whereas arterioles from wild-type *Cav1*$^{+/+}$ and heterozygous *Cav1*$^{+/-}$ mice dilated robustly (Fig. 2a, c, e, Extended Data Fig. 3a, i, Supplementary Video 4). Moreover, this vasodilation defect was observed in both pial arteries and penetrating arterioles diving deep into the parenchyma in *Cav1*$^{-/-}$ mice compared with their wild-type littermates (Extended Data Fig. 2). Notably, the baseline diameter and latency to dilate were similar across the three genotypes (Extended Data Fig. 3b–d). These results suggest that the absence of caveolae does not impair basal vessel tone and kinetics but specifically impairs the amplitude of sensory-evoked arteriolar dilation. Consistent with the attenuation of arteriolar vasodilation, capillary blood flow was also impaired in mutant *Cav1*$^{-/-}$ mice upon whisker stimulation compared to control mice (Fig. 2b, d, f, Supplementary Video 5), whereas baseline capillary velocity and kinetics were similar across genotypes (Extended Data Fig. 3e, f). Moreover, the attenuated arteriolar dilation and capillary blood flow in mutant *Cav1*$^{-/-}$ mice were not due to either the impairment in sensory-evoked neural activity or alteration in blood pressure, because control and mutant mice display similar GCaMP6s dynamics in neurons (Extended Data Fig. 3g, h) and similar systolic, diastolic and mean blood pressure (Extended Data Fig. 3j). The normal blood pressure observed in *Cav1*$^{-/-}$ mutant mice is consistent with previous studies[18]. Thus, these results demonstrate that caveolae are essential for optimal neurovascular coupling.

Because SMCs control arteriolar dilation during neurovascular coupling[2,4], we next examined whether the attenuated neurovascular coupling in *Cav1*$^{-/-}$ mice is due to impaired integrity and function of SMCs. To visualize SMC morphology and vessel coverage, we intravenously injected hydrazide into control *Cav1*$^{+/+}$*;NG2*-DsRed^{+} and mutant *Cav1*$^{-/-}$*;NG2*-DsRed^{+} mice. *NG2*-DsRed is a reporter for SMCs, oligodendrocytes and pericytes[16,19]. By quantifying of the number of DsRed^{+} cells on hydrazide^{+} arterioles, we established that there is normal coverage and morphology of SMCs in *Cav1*$^{-/-}$ mice compared with wild type (Extended Data Fig. 4a, b). Moreover, we found similar expression of various contractile proteins, including α-smooth muscle actin (SMA), MYH11, transgelin and desmin in SMCs in *Cav1*$^{-/-}$ mice and wild-type littermates (Extended Data Fig. 4c–g).

To examine whether ablation of caveolae affects the ability of SMCs to respond to contractile and vasodilatory signals, we imaged arteriolar diameter changes in acute brain slices under two-photon microscopy after delivery of contractile and vasodilatory pharmacological compounds. We found that SMCs in *Cav1*$^{-/-}$ mice displayed normal contraction compared with wild-type controls following administration of U46619, a thromboxane A2 receptor agonist (Extended Data Fig. 4h, i, Supplementary Videos 6, 7). When diethylamine (DEA)-NONOate, a NO donor, was subsequently applied to the same vessel, we observed a similar level of dilation as in the wild-type controls (Extended Data Fig. 4h, j, Supplementary Videos 6, 7). Finally, to examine whether the impaired neurovascular coupling in mutant *Cav1*$^{-/-}$ mice is due to the inability of SMCs to relax following release of vasodilatory signals in vivo, we used two-photon microscopy in anaesthetized mice and imaged changes in vasodilation upon superfusing DEA NONOate onto the pia of control *Cav1*$^{+/+}$ and mutant *Cav1*$^{-/-}$ mice. Upon acute administration of DEA NONOate, the SMCs from both control *Cav1*$^{+/+}$ and mutant *Cav1*$^{-/-}$ mice relax and dilate arterioles at similar levels in vivo (Extended Data Fig. 4k, l, Supplementary Videos 8, 9). These experiments demonstrate that the absence of caveolae impairs neurovascular coupling despite the presence of functionally normal SMCs.

Neurovascular coupling requires aEC caveolae

Caveolae are present in both aECs and SMCs in the CNS (Fig. 1c, f). We next tested whether caveolae function in a cell-autonomous manner using acute, cell-type-specific deletion of *Cav1* in adult mice. First, we crossed *BMX*^{creER} mice, a tamoxifen-inducible aEC-specific driver line[20], with *Cav1*-floxed mice (*Cav1*$^{fl/fl}$)[21] to acutely ablate caveolae only in aECs. After tamoxifen treatment, CAV1 was specifically lost in aECs but not in SMCs of *BMX*$^{creER+}$*;Cav1*$^{-/fl}$ mutant mice; CAV1 protein was present in both aECs and SMCs in *BMX*$^{creER-}$*;Cav1*$^{+/fl}$ control mice. (Extended Data Fig. 5a, c). Transmission electron microscopy analysis showed that in the barrel cortex of mutant *BMX*$^{creER+}$*;Cav1*$^{-/fl}$ mice, caveolae were ablated acutely in aECs but were still present in SMCs, whereas abundant caveolae were present in both aECs and SMCs in the CNS of control *BMX*$^{creER-}$*;Cav1*$^{+/fl}$ mice (Extended Data Fig. 5b, d). Using our in vivo imaging paradigm, we found attenuation in arteriolar dilation (Fig. 2g, i, Extended Data Fig. 6a) and capillary blood flow (Fig. 2h, j) in *BMX*$^{creER+}$*;Cav1*$^{-/fl}$ mice on whisker stimulation, similar to observations in the *Cav1*$^{-/-}$ mutant mice (Fig. 2a–f). Baseline and kinetics of arteriolar diameter and capillary blood flow were unaffected in tamoxifen-treated *BMX*$^{creER+}$*;Cav1*$^{-/fl}$ mice (Extended Data Figs. 5e, f, 6b–d). Together, these experiments demonstrate that caveolae in aECs are important for neurovascular coupling.

SMC caveolae are dispensable

To test the role of SMC caveolae in neurovascular coupling, we crossed *Myh11*$^{creER+}$ mice, a tamoxifen-inducible SMC driver line[22], to *Cav1*-floxed mice to acutely ablate caveolae in SMCs. After tamoxifen treatment, we found that both CAV1 protein and caveolae were ablated successfully in SMCs but preserved in aECs in *Myh11*$^{creER+}$*;Cav1*$^{-/fl}$ mutant mice (Extended Data Fig. 7a–d). However, in contrast to the attenuated neurovascular coupling observed in mice lacking CAV1 in aECs, no impairment in arteriolar dilation and capillary blood flow after whisker stimulation were observed in mutants lacking CAV1 and caveolae in SMCs (Extended Data Figs. 6e–h, 7e–j), indicating that caveolae in SMCs have a negligible role—if any—in neurovascular coupling.

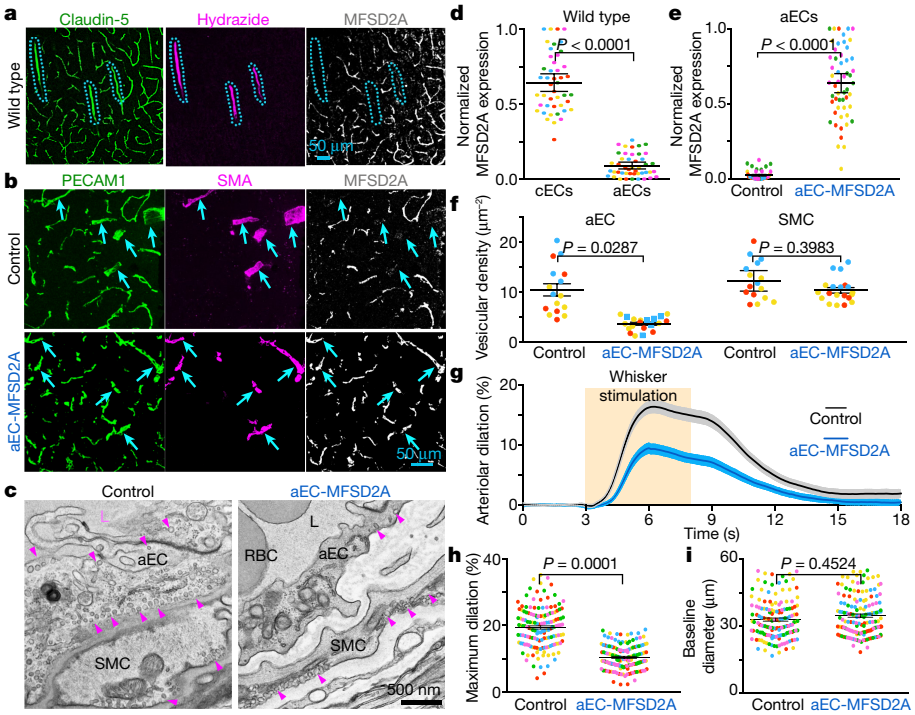

Fig. 4 | CNS arterioles do not express MFSD2A and ectopic expression of MFSD2A in aECs downregulates caveolae and attenuates neurovascular coupling. a, Immunostaining for claudin 5, hydrazide and MFSD2A on wild-type adult brain sections demonstrates that MFSD2A is not detectable in CNS arterioles. Blue hashes outline the hydrazide$^+$ arterioles. **b**, Immunostaining on adult brain sections for PECAM1, SMA and MFSD2A from control (BMX^{creER-};$R26^{LSL\text{-}Mfsd2a/+}$) mice and mice overexpressing MFSD2A specifically in the aEC (BMX^{creER+};$R26^{LSL\text{-}Mfsd2a/+}$). Arrowheads point to SMA$^+$ arteries. **d**, Quantification of the normalized immunofluorescence of MFSD2A in cECs (hydrazide$^-$claudin 5$^+$) and aECs (hydrazide$^+$claudin 5$^+$) ($n = 5$ mice, 45 images) as shown in **a**. **e**, Normalized MFSD2A immunofluorescence in aECs from control mice ($n = 4$ mice, 40 images) and mice overexpressing MFSD2A specifically in the aEC ($n = 5$ mice, 51 images) as shown in **b**. **c**, **f**, Transmission electron microscopy images of CNS aECs and SMCs (**c**) and quantification of the mean vesicular density (**f**) in aECs and SMCs from control mice ($n = 3$ mice, 20 arterioles) and mice overexpressing MFSD2A specifically in the aEC ($n = 3$ mice, 22 arterioles). Arrowheads point to caveolae. **g**–**i**, Time course of change in arteriolar dilation (**g**) and maximum percentage change in arteriolar dilation (**h**) and baseline diameter (**i**) in control mice ($n = 7$ mice, 260 arterioles) and mice overexpressing MFSD2A specifically in the aEC ($n = 5$ mice, 193 arterioles. Data are mean ± s.e.m.; nested, unpaired, two-tailed *t*-test (**d**–**f**, **h**, **i**).

Caveolae in aECs function independently of eNOS

Next, we examined how aECs utilize caveolae to mediate neurovascular coupling. Caveolae have been implicated in many cellular processes[23], including transcytosis[11,12], serving as a membrane reservoir during mechanical stretch[24], clustering receptors and ion channels[25], and mediating intracellular signalling[26]. We focused on NO signalling because NO is a major vasodilatory factor in neurovascular coupling[27] and previous studies have reported that CAV1 interacts physically with eNOS (encoded by *Nos3*)[28]. We first examined whether eNOS and NO levels are altered in the absence of caveolae. Unexpectedly, we found similar levels of eNOS protein and NO in aECs in wild-type control and $Cav1^{-/-}$ mice, whereas both eNOS protein and NO signal were absent in $Nos3^{-/-}$ mice (Extended Data Fig. 8a–d). To examine genetic interactions between *Cav1* and *Nos3*, we characterized neurovascular coupling in $Cav1^{-/-}Nos3^{-/-}$ double-mutant mice. We reasoned that if CAV1 and eNOS are in the same genetic pathway, the double mutants should phenocopy one of the single knockout mice, whereas if they function in separate parallel pathways, the double knockout should have an additive phenotype of the two single-knockout mice. Using our in vivo imaging paradigm, $Nos3^{-/-}$ mice displayed attenuated arteriolar dilation and capillary blood flow upon whisker stimulation (Fig. 3a–d), consistent with a previous report[27]. The $Cav1^{-/-}Nos3^{-/-}$ double mutant mice completely lost arteriolar dilation and red blood cell velocity enhancement upon whisker stimulation, compared with a partial reduction in $Cav1^{-/-}$ and $Nos3^{-/-}$ single mutants despite having normal baseline diameter and blood flow (Fig. 3a–d, Extended Data Fig. 8e, f). These results demonstrate that caveolae-mediated neurovascular coupling is independent of the NO pathway. Moreover, the caveolae-mediated pathway is at least as important as the NO pathway for neurovascular coupling.

MFSD2A downregulates neurovascular coupling

We next investigated why cECs have few caveolae whereas aECs have abundant caveolae. It was previously discovered that MFSD2A expression in CNS cECs actively suppressed caveolae formation and that this was necessary for blood–brain barrier integrity[10–12]. Using immunohistochemistry, we found that MFSD2A protein was undetectable in aECs in both brain and retina (Fig. 4a, d, Extended Data Fig. 9a–d). Consistent with this result, *Mfsd2a* transcript levels are also low in aECs compared with cECs[29]. Thus, CNS cECs robustly express *Mfsd2a* to suppress caveolae, whereas aECs lack MFSD2A and are enriched in caveolae. We therefore examined whether ectopic expression of *Mfsd2a* specifically in CNS aECs is sufficient to suppress caveolae in these cells; if so, our results so far predict that this suppression of caveolae in aECs would result in an attenuated neurovascular coupling.

To ectopically express *Mfsd2a* in aECs only, we generated a transgenic mouse in which *Mfsd2a* expression is Cre-dependent (referred to as $R26^{LSL\text{-}Mfsd2a}$) (Extended Data Fig. 10a, b) and crossed it to BMX^{creER+}. After tamoxifen treatment, MFSD2A protein was expressed abundantly in aECs in brains from BMX^{creER+};$R26^{LSL\text{-}Mfsd2a/+}$ mice, whereas control BMX^{creER-};$R26^{LSL\text{-}Mfsd2a/+}$ adult mice lacked MFSD2A expression in brain arterioles (Fig. 4b, e). Moreover, electron microscopy analysis revealed that caveolae density was reduced significantly in BMX^{creER+};$R26^{LSL\text{-}Mfsd2a/+}$ mice relative to control (Fig. 4c, f). Of note, in vivo imaging revealed an attenuation of arteriolar dilation upon whisker stimulation in mice with MFSD2A overexpression in aECs (BMX^{creER+};$R26^{LSL\text{-}Mfsd2a/+}$) relative

to control mice (*BMX*$^{creER-}$;*R26*$^{LSL\text{-}Mfsd2a/+}$) (Fig. 4g–i, Extended Data Fig. 10e). These experiments demonstrate that ectopic overexpression of MFSD2A in CNS aECs is sufficient to reduce caveolae density and impair neurovascular coupling. Furthermore, inhibition of caveolae vesicles specifically in aECs using two different approaches (overexpression of MFSD2A and genetic deletion of *Cav1*) both resulted in attenuated neurovascular coupling, demonstrating the importance of caveolae in CNS aECs for mediating neurovascular coupling.

Discussion

We used natural stimuli under physiological conditions in awake mice while simultaneously measuring neural activity and vascular dynamics under two-photon microscopy to study mechanisms underlying neurovascular coupling. We discovered that caveolae in CNS aECs have a key role in mediating neurovascular coupling. In addition, we confirmed that the previously reported eNOS pathway also has a role in neurovascular coupling[27]. However, we found that the caveolae-mediated pathway is independent of eNOS signalling, as the perturbation of both caveolae- and eNOS-mediated pathways together completely abolished neurovascular coupling, whereas ablation of each pathway alone resulted in partial impairment. Thus, these findings indicate that the caveolae-mediated pathway is at least as important as the NO pathway for neurovascular coupling.

Previous studies highlighted the importance of ECs in neurovascular coupling in vivo. Locally disrupting ECs using optically induced reactive oxygen species halted propagation of stimulus-evoked vasodilation in pial arteries[6]. Our present findings have extended this work to identify and demonstrate specific molecular and subcellular components in aECs that are essential for neurovascular coupling using cell-type-specific genetic manipulations. Given the recent evidence that cECs are involved in sensing neural activity changes and are important for neurovascular coupling[2,6,8], we propose that after sensing nearby increased neural activity, cECs relay this signal electrically to the upstream aECs, which in turn send vasodilatory cues to SMCs via a caveolae-dependent process. We considered how caveolae could carry out this function. Although caveolae have been reported to serve as a membrane reservoir during mechanical stretch[24], the attenuated vasodilation observed in *Cav1*$^{-/-}$ mice is unlikely to result from impaired arteriolar elasticity, given that superfusing NO donor in vivo—which dilates arterioles by directly relaxing SMC—produced similar dilations in wild-type and *Cav1*$^{-/-}$ mice (Extended Data Fig. 4k, l, Supplementary Videos 8,9). Similarly, previously described interactions between caveolae and the eNOS-signalling pathway cannot explain the impaired vasodilation observed in *Cav1*$^{-/-}$ mutant mice, because simultaneous ablation of both caveolae- and eNOS-mediated pathways abolishes neurovascular coupling, whereas ablation of either pathway alone results in only partial impairment. In light of these results, the ability of caveolae to cluster ion channels and receptors[30]—several of which have been implicated in vasodilation[8]—probably explains its role in neurovascular coupling. In aECs, caveolae could cluster these channels to facilitate transmission of vasodilatory signals to SMCs. Identifying the channels that cluster in caveolae in aECs will be an important next step for the field to address.

Our results also demonstrate that ECs from different vascular segments in the CNS exhibit heterogeneity at molecular, cellular and functional levels. Here we show that this endothelial heterogeneity governs the two unique and important functions of the CNS vasculature: the blood–brain barrier and neurovascular coupling. We found that cECs express MFSD2A, which suppresses caveolae to ensure blood–brain-barrier integrity[10–12]. By contrast, aECs lack MFSD2A and concurrently have abundant caveolae, which are important for neurovascular coupling. We expect this kind of heterogeneity to exist broadly in CNS ECs and that understanding this heterogeneity will advance our understanding of the diverse functions of ECs in health and disease. Given that neurovascular coupling is impaired in various neurological disorders[1], future studies examining whether these different molecular and cellular pathways are altered in disease may provide insight for development of novel therapies.

Online content

Any methods, additional references, Nature Research reporting summaries, source data, extended data, supplementary information, acknowledgements, peer review information; details of author contributions and competing interests; and statements of data and code availability are available at https://doi.org/10.1038/s41586-020-2026-1.

1. Iadecola, C. The neurovascular unit coming of age: a journey through neurovascular coupling in health and disease. *Neuron* **96**, 17–42 (2017).
2. Hillman, E. M. C. Coupling mechanism and significance of the BOLD signal: a status report. *Annu. Rev. Neurosci.* **37**, 161–181 (2014).
3. Sweeney, M. D., Sagare, A. P. & Zlokovic, B. V. Blood–brain barrier breakdown in Alzheimer disease and other neurodegenerative disorders. *Nat. Rev. Neurol.* **14**, 133–150 (2018).
4. Kleinfeld, D. et al. A guide to delineate the logic of neurovascular signaling in the brain. *Front. Neuroenergetics* **3**, 1 (2011).
5. Shen, Z., Lu, Z., Chhatbar, P. Y., O'Herron, P. & Kara, P. An artery-specific fluorescent dye for studying neurovascular coupling. *Nat. Methods* **9**, 273–276 (2012).
6. Chen, B. R., Kozberg, M. G., Bouchard, M. B., Shaik, M. A. & Hillman, E. M. C. A critical role for the vascular endothelium in functional neurovascular coupling in the brain. *J. Am. Heart Assoc.* **3**, e000787 (2014).
7. O'Herron, P. et al. Neural correlates of single-vessel haemodynamic responses in vivo. *Nature* **534**, 378–382 (2016).
8. Longden, T. A. et al. Capillary K$^+$-sensing initiates retrograde hyperpolarization to increase local cerebral blood flow. *Nat. Neurosci.* **20**, 717–726 (2017).
9. Hogan-Cann, A. D., Lu, P. & Anderson, C. M. Endothelial NMDA receptors mediate activity-dependent brain hemodynamic responses in mice. *Proc. Natl Acad. Sci. USA* **116**, 10229–10231 (2019).
10. Ben-Zvi, A. et al. Mfsd2a is critical for the formation and function of the blood–brain barrier. *Nature* **509**, 507–511 (2014).
11. Chow, B. W. & Gu, C. Gradual suppression of transcytosis governs functional blood–retinal barrier formation. *Neuron* **93**, 1325–1333.e3 (2017).
12. Andreone, B. J. et al. Blood–brain barrier permeability is regulated by lipid transport-dependent suppression of caveolae-mediated transcytosis. *Neuron* **94**, 581–594.e5 (2017).
13. Razani, B. et al. Caveolin-1 null mice are viable but show evidence of hyperproliferative and vascular abnormalities. *J. Biol. Chem.* **276**, 38121–38138 (2001).
14. Drab, M. et al. Loss of caveolae, vascular dysfunction, and pulmonary defects in caveolin-1 gene-disrupted mice. *Science* **293**, 2449–2452 (2001).
15. Simionescu, M. et al. The cerebral microvasculature of the rat: structure and luminal surface properties during early development. *J. Submicrosc. Cytol. Pathol.* **20**, 243–261 (1988).
16. Hill, R. A. et al. Regional blood flow in the normal and ischemic brain is controlled by arteriolar smooth muscle cell contractility and not by capillary pericytes. *Neuron* **87**, 95–110 (2015).
17. Lim, D. H. et al. In vivo large-scale cortical mapping using channelrhodopsin-2 stimulation in transgenic mice reveals asymmetric and reciprocal relationships between cortical areas. *Front. Neural Circuits* **6**, 11 (2012).
18. Rosengren, B.-I. et al. Transvascular protein transport in mice lacking endothelial caveolae. *Am. J. Physiol. Heart Circ. Physiol.* **291**, H1371–H1377 (2006).
19. Zhu, X., Bergles, D. E. & Nishiyama, A. NG2 cells generate both oligodendrocytes and gray matter astrocytes. *Development* **135**, 145–157 (2008).
20. Ehling, M., Adams, S., Benedito, R. & Adams, R. H. Notch controls retinal blood vessel maturation and quiescence. *Development* **140**, 3051–3061 (2013).
21. Asterholm, I. W., Mundy, D. I., Weng, J., Anderson, R. G. W. & Scherer, P. E. Altered mitochondrial function and metabolic inflexibility associated with loss of caveolin-1. *Cell Metab.* **15**, 171–185 (2012).
22. Wirth, A. et al. G12–G13–LARG-mediated signaling in vascular smooth muscle is required for salt-induced hypertension. *Nat. Med.* **14**, 64–68 (2008).
23. Parton, R. G. Caveolae: structure, function, and relationship to disease. *Annu. Rev. Cell Dev. Biol.* **34**, 111–136 (2018).
24. Sinha, B. et al. Cells respond to mechanical stress by rapid disassembly of caveolae. *Cell* **144**, 402–413 (2011).
25. Balijepalli, R. C. & Kamp, T. J. Caveolae, ion channels and cardiac arrhythmias. *Prog. Biophys. Mol. Biol.* **98**, 149–160 (2008).
26. Sowa, G., Pypaert, M. & Sessa, W. C. Distinction between signaling mechanisms in lipid rafts vs. caveolae. *Proc. Natl Acad. Sci. USA* **98**, 14072–14077 (2001).
27. Toth, P. et al. Purinergic glio-endothelial coupling during neuronal activity: role of P2Y1 receptors and eNOS in functional hyperemia in the mouse somatosensory cortex. *Am. J. Physiol. Heart Circ. Physiol.* **309**, H1837–H1845 (2015).
28. García-Cardeña, G. et al. Dissecting the interaction between nitric oxide synthase (NOS) and caveolin. Functional significance of the nos caveolin binding domain in vivo. *J. Biol. Chem.* **272**, 25437–25440 (1997).
29. Vanlandewijck, M. et al. A molecular atlas of cell types and zonation in the brain vasculature. *Nature* **554**, 475–480 (2018).
30. Goedicke-Fritz, S. et al. Evidence for functional and dynamic microcompartmentation of Cav-1/TRPV4/K_{Ca} in caveolae of endothelial cells. *Eur. J. Cell Biol.* **94**, 391–400 (2015).

Methods

Mice

All mouse experiments were approved by the Harvard University Institutional Animal Care and Use Committee (IACUC). The following mice strains were used: wild type (C57BL/6J, Jackson Laboratory, no. 000664), *Mfsd2a*^{creER} (ref. [31]), *BMX*^{creER} (ref. [20]), *Myh11*^{creER} (ref. [22]), *NG2-DsRED* (ref. [19]; JAX, no. 008241), *Ai14* (ref. [32]; JAX, no. 007914), *Ai39* (ref. [33]; JAX, no. 014539), *Ai75* (ref. [34]; JAX, no. 014539), *ROSA26*$^{LSL\text{-}Mfsd2a}$ (generated during this study), *Thy1*-GCaMP6s[35] (JAX, no. 024275), *Cav1*$^{-/-}$ [13] (JAX, no. 007083), *Cav1*-floxed[21], *Nos3*$^{-/-}$ [36] (JAX, no. 002684), ROSA26-PhiC31 (ref. [37]; JAX, no. 007743). All mice were maintained on a mixed background and both males and females were used. For adult mice expressing *creER*, tamoxifen (Sigma-Aldrich, T5648) was dissolved in corn oil at a concentration of 20 mg ml^{-1} and injected into peritoneal cavities with 0.2 mg g^{-1} body weight. Six- to seven-week-old mice were treated with tamoxifen for five consecutive days and were allowed to recover for one week following the last tamoxifen treatment before cranial surgery or dissections were performed. Randomization was determined by mouse genetics as wild types, mutants and transgenic mice were assigned randomly into their respective genotype group. Sample sizes were determined by a power calculation on the basis of previous pilot data and representative sample sizes from previous literature that had similar experiments. In experiments involving mutant and transgenic mice, the genotypes were blinded until after data acquisition and analysis.

Generation of *ROSA26-LSL-Mfsd2a* transgenic mice

The targeting vector contains a CAG promoter and loxP-3×SV40PA-loxP followed by mouse *Mfsd2a* cDNA and WPRE-PolyA. A positive selection cassette, attB-PGKNeoR-attP, is located between the insertion and the 3′ homologous arm which is 4.3 kb. The length of the 5′ homologous arm is 1.1 kb (Extended Data Fig. 10).

The targeting vector was electroporated into embryonic stem (ES) cells derived from F_1 hybrid blastocyst of 129S6 × C57BL/6J. The G418-resistant ES clones were screened by nested PCR using primers outside the construct paired with primers inside the insertion cassette. The positive ES cell clones were used to generate chimeric mice by aggregating with 8-cell embryos of CD-1 strain. The attB-Neo-attP cassette was removed in mice by crossing the chimaeras with R26PhiC31 females (JAX, no. 007743) backcrossed in C57BL/6J for 13 generations. The F_1 pups were genotyped by PCR using primers set (5′-CCAAAGTCGCTCTGAGTTGT-3′); (5′-CCAGGTTAGCCTTTAAGCCT-3′) and (5′-CGGGCCATTTACCGTAAGTT-3′). The PCR products are 250 bp for the wild-type allele and 329 bp for the mutant allele.

Long-term cranial window surgery

Six-week- to four-month-old mice underwent a craniotomy, implantation of a sterile glass window (3.0 mm) and attachment of a customized titanium head plate to the skull using dental cement (Metabond Parkell). Prior to the craniotomy, an intramuscular dose of dexamethasone (120 mg kg^{-1}) was administered. Mice were anaesthetized with 3–5% isoflurane and maintained at 1–2% isoflurane for the duration of the craniotomy. The respiration rate and body temperature were continuously monitored throughout the procedure to ensure the appropriate level of anaesthesia. A subcutaneous dose of the analgesic: buprenorphine (0.1 mg kg^{-1}) and ketoprofen (5.0 mg kg^{-1}) was administered at the onset of the procedure and was also administered daily for two additional days after the craniotomy. A single dose of the local anaesthetic lidocaine (20 mg kg^{-1})/bupivacaine (2.5 mg kg^{-1}) was administered subcutaneously at the site of the craniotomy. The centre of the craniotomy over the barrel cortex and retrosplenial cortex was determined for each mouse in relation to the skull indentations bregma and lambda. Generally, for barrel cortex surgery, 3.5–3.8 mm posterior and 1.5 mm laterally from the midpoint between bregma and lambda along the sagittal suture was marked as the centre of the craniotomy. For retrosplenial cortex surgery, the centre of the craniotomy was 3.2–3.5 mm posterior and 1.0 mm lateral from bregma. Following the craniotomy and the window with head plate implantation, mice were treated with buprenorphine/ketoprofen and observed for signs of pain and/or infection for 72 h. Furthermore, mice were handled by the experimenter, habituated to head restraint and trained to run on a foam ball daily for three consecutive days. Sensory-evoked arteriolar dilation and capillary blood flow were imaged through a 3.0-mm-diameter cranial window positioned over the somatosensory cortex in head-restrained mice with the freedom to walk on a bidirectional styrofoam ball.

Two-photon microscopy

Two-photon imaging was performed using a custom-built microscope equipped with a tunable Ti:sapphire laser (MaiTai HP DS, Spectra-Physics) controlled by ScanImage 5.1 (Vidrio Technologies). The intensity of the femtosecond pulsed infrared beam was controlled by an electro-optical modulator (Conoptics) and passed through a pair of scan mirrors (Cambridge Technology) that enabled image acquisition at 30 Hz for a field of view of 1.0 mm^2 and 512 × 512 pixels. Control of image zoom was enabled by controlling the resonant scanner amplitude. The objective lens used was a 16×, 0.8 NA, water-immersion lens (Nikon). Green and red fluorescence photons were separated using a custom-sized dichroic beamsplitter (580 BrightLine, Semrock) and two custom-sized single-band bandpass filters (525/50 nm BrightLine, 641/75 nm BrightLine, Semrock). Fluorescence photons were collected using photomultiplier tubes (Hamamatsu).

In vivo imaging of pial arteriolar dilation and analysis

Arterioles labelled with Alexa Fluor Hydrazide 633 were imaged at 800 nm with a field of view size of 200 μm × 200 μm (512 × 512 pixels, pixel size of 0.16 μm^2 per pixel) at 30 Hz. Whisker stimulation (4 Hz, 5 s) was performed using a foam brush controlled by a servo motor under the control of WaveSurfer. Alexa Fluor 633 Hydrazide (5 mg kg^{-1}) was intravenously injected into mice to visualize arterioles in vivo[5]. We imaged surface-level pial arteries and arterioles from the middle cerebral artery. Our selection of arteries and arterioles were guided by hydrazide$^+$ vessels, which labels arteries and arterioles only[5,7]. Because we are stimulating the entire whisker pad (Extended Fig. 1) as opposed to stimulating individual whiskers, we observed changes in all sampled branches. This is consistent with previous findings[16] that branch orders were not necessarily relevant as long as the vessels were arterial (which they defined as SMA$^+$ or hydrazide$^+$). Three technical trials were acquired and averaged for each field of view. Ten to thirteen fields of view were acquired per imaging session. Three imaging sessions were collected on three separate days per mouse and arteriolar dilation responses were averaged across all three sessions for each mouse. To determine per cent change in diameter relative to baseline, the time series were first filtered with a Gaussian blur and background subtracted with a rolling ball of 50 pixels. Five-line scans orthogonal to the arterioles were sampled to generate kymographs. The two maximum intensity peaks (which represent the walls of the arterioles) were identified across the kymograph. The change in diameter of the arterioles was determined as $(\text{diameter}_{\text{time}} - \text{diameter}_{\text{baseline}})/\text{diameter}_{\text{baseline}}$. $\text{Diameter}_{\text{baseline}}$ was determined as the mean diameter during the 3 s before the whisker stimulation. $\text{Diameter}_{\text{time}}$ is the vessel diameter at a particular time. The change in maximum diameter was determined as the maximum value during the whisker stimulation. To determine latency onset to dilate, a line was fitted through 80% and 20% of the maximum value. The latency onset to dilate was considered the time difference between the *x*-intercept of the line and the start of the whisker stimulation.

In vivo imaging of parenchymal arteriolar dilation and analysis

Arterioles stained with Alexa Fluor 633 Hydrazide (5 mg kg^{-1}) were imaged at multiple depths within the barrel cortex. Three parenchymal

depths were used at 100 µm, 200 µm and 300 µm from the pial surface. Three technical trials were acquired and averaged for each field of view at each depth location. Three-to-four diving arterioles were imaged per imaging session and three sessions on sequential days were recorded in total per mouse. For analysis of parenchymal arterial dilation which appear as ellipses, we tracked the diving arterioles by fitting an ellipse to the hydrazide signal. Movies were first averaged using a three-frame rolling average then smoothed with a Laplacian of Gaussian filter. Intensities of the smoothed movie were rescaled to range from 0 to 255 and a threshold pixel intensity was picked to exclude background fluorescence signal outside of the ring of hydrazide signal surrounding the arteriole. Next, ridge detection was performed using the FIJI ridge detection plugin[38]. Three separate ridge-detection parameter sets were used and the ridges were combined to detect bright and dim ridges. Next, an initial estimate of the ellipse fit was determined using an elliptical Hough transform on the binarized ridge image. The fit was then refined by minimizing the distance between the ridge pixels and the fitted ellipse using the Hough transform results as the starting parameter values. The ellipse was parameterized as follows:

$$x(\alpha) = a\cos(\alpha)\cos(\theta) - b\sin(\alpha)\sin(\theta) + x_o$$

$$y(\alpha) = a\cos(\alpha)\sin(\theta) - b\sin(\alpha)\cos(\theta) + y_o$$

in which $x(\alpha)$, $y(\alpha)$ are the x and y coordinates of the points on the ellipse, a and b are the two ellipse axes, θ is the tilt angle of the ellipse, x_o and y_o are the coordinates of the ellipse centre, and α ranges from 0 to 2π to circumscribe the entire ellipse perimeter. Minimization was done in MATLAB using the lsqnonlin function and 95% confidence intervals of the parameters were determined using nlparci. To be consistent with the pial artery dilation tracking, we report changes in diameter of the parenchymal arterioles ($\Delta D/D_{baseline}$) from the minor axis of the ellipse, which does not depend on the orientation of the arteriole cross section relative to the microscope optical axis. As image quality is variable, frames with poor accuracy fitting are discarded by first rejecting frames in which the minor axis fit is more than two median absolute deviations from the ten-frame sliding window median. Next, frames that have a confidence interval greater than four pixels for the minor axis are discarded. If fewer than 50% of the frames of the trajectory remain, the entire trajectory is discarded. Finally, the trajectory was smoothed using the MATLAB smooth function with rlowess. To obtain $\Delta D/D_{baseline}$, this value was multiplied by two and divided by the mean diameter immediately 3 s before whisker stimulation. The three technical replicates were averaged as with the pial artery dilation experiments to produce the trajectory for the vessel.

In vivo imaging of capillary red blood cell velocity and analysis

Mice were intravenously injected with quantum dots 525 (Thermo Fisher Scientific) and Alexa Fluor Hydrazide 633 to unambiguously distinguish arterioles and capillaries in vivo. Hydrazide-negative capillaries were imaged with a field of view size of 100 µm × 25 µm (512 × 25 pixels, pixel size of 0.04 µm^2 per pixel) at 610 Hz. Whisker stimulation (4 Hz, 5 s) was performed using a foam brush controlled by a servo motor under the control of Wavesurfer. Three technical trials were acquired and averaged for each field of view. Three imaging sessions were collected on three separate days per mouse and changes in capillary red blood cell velocity were averaged across all three sessions for each mouse. To determine per cent change in velocity relative to baseline, the movies were first filtered with a Gaussian blur and background subtracted with a rolling ball of 50 pixels. Five-line scans parallel to the flow of red blood cells were sampled to generate kymographs. Using a published algorithm[39] that uses an iterative radon transform and edge detection filter, the change in velocity of red blood cells was determined as $(velocity_{time} - velocity_{baseline})/velocity_{baseline}$. Velocity baseline was defined as the mean velocity during the 3 s before the whisker stimulation. $Velocity_{time}$ is the velocity of the red blood cell flow at that moment in time The change in maximum velocity was determined as the maximum value during the whisker stimulation. To determine latency onset to increase red blood cell velocity, a line was fitted through 80% and 20% of the maximum velocity value. The latency onset was considered the time difference between the x intercept of the fitted line and the start time of the whisker stimulation.

In vivo two-photon imaging and pharmacology

To assess vasodilatory function of pial artery SMCs, we imaged pial artery diameter changes with two-photon microscopy in response to topical application of the nitric oxide donor DEA NONOate (EMD Millipore). Arteries were stained with Alexa Fluor 633 Hydrazide, as described earlier, one day before the imaging session. Under isoflurane anaesthesia (1.0–1.5%), a titanium head-plate with a 10-mm-diameter hole centred over the right parietal skull bone was cemented onto the skull using Metabond. A custom perfusion system was constructed along the rim of the head-plate hole to allow for simultaneous imaging and application of DEA NONOate. A 5.0–7.0-mm circular craniotomy of the right parietal skull bone was carefully performed and the newly exposed cortex was kept submerged in artificial cerebral spinal fluid (aCSF) for the duration of the experiment. The mouse was then carefully transitioned from isoflurane (0.5%) to ketamine/xylazine (100 mg kg^{-1}) and transferred from the surgical stereotaxic stage to the imaging platform where body temperature was maintained at 37 °C using a heat pad. A fresh 1.0 µM DEA NONOate solution was prepared immediately before the start of the imaging session given the short half-life of DEA NONOate in aqueous solution. A syringe pump (Harvard Apparatus) controlled the application of the DEA NONOate solution onto the exposed cortex at 1.0 ml min^{-1}. Five recordings (30 s in duration) of each pial vessel per mouse where collected in series interleaved with 30 s of washing with aCSF. The five measurements were then averaged per mouse.

Ex vivo, acute slice two-photon slice imaging and pharmacology

Acute coronal brain slices were prepared by deeply anaesthetizing mice with isoflurane inhalation followed cardiac perfusion with ice-cold choline-based cut solution containing (in mM): 25 $NaHCO_3$, 25 glucose, 1.25 NaH_2PO_4, 7 $MgCl_2$, 2.5 KCl, 0.5 $CaCl_2$, 11.6 ascorbic acid, 3.1 pyruvic acid and 110 choline chloride. After brain dissection and blocking, 300-µm slices were prepared in cut solution with a Leica VT1000 s vibratome. Slices were then transferred for 30 min to recovery into a holding chamber containing 34 °C (aCSF) containing (in mM): 125 NaCl, 2.5 KCl, 1.25 NaH_2PO4, 25 $NaHCO_3$, 11 glucose, 2 $CaCl_2$ and 1 $MgCl_2$. During recovery, slices were incubated with approximately 1 µM Alexa Fluor 633 Hydrazide (ThermoFisher). Following recovery, slices were imaged while constantly perfused with room temperature aCSF. Choline cut solution and aCSF were constantly bubbled with 5% CO_2/95% O_2. Imaging was performed on a custom-built two-photon microscope and images acquired with a custom version of ScanImage written in MATLAB (Mathworks). During imaging, arteries were constricted with 100 nM U46619 (Sigma-Aldrich) and dilated by acutely dissolving about 5 mg of DEA NONOate (EMD Millipore) into the 10 ml of recycling aCSF being perfused over the slice.

Non-invasive blood pressure measurement procedure in awake mice

Systolic, diastolic and mean blood pressure were measured using the non-invasive tail-cuff method (CODA Monitor, Kent Scientific). At the start of a blood pressure measurement session, the appropriate mouse holder was selected on the basis of the mouse's weight. The holder was placed over a heating pad with a set temperature that is regulated at 38 °C. The tail-cuff and volume pressure recording sensor were placed on the heating pad and covered with a blanket to allow these components to reach the set temperature. After 2–3 min, the awake mouse was gently introduced into the holder. A light blanket was draped over

the tail and the mouse was left alone for 3–5 min to allow habituation. The blood pressure measurements take place via 10–20 tail-cuff inflation–deflation sweeps that in total take from 5–10 min in duration. Multiple days of measurements may be required to gain confidence in the accuracy of the measurements. After the measurements, the mouse was carefully removed from the holder and immediately placed in its cage. Measurements of all sweeps are then averaged per mouse.

SMC coverage quantification

NG2^{DsRED} (or *CSPG4*^{DsRED}) mice were crossed to *Cav1*$^{-/-}$ mice. Cranial window surgeries were performed over the barrel cortex of *Cav1*$^{+/+}$;*NG2*$^{DsRED+}$ and *Cav1*$^{-/-}$;*NG2*$^{DsRED+}$ mice. Mice were injected with Alexa Fluor 488 Hydrazide (5 mg kg^{-1}). Around 30 arterioles (hydrazide^{+}DsRed^{+}) per mouse were imaged. A 100-µm intensity line profile was drawn perpendicularly to the contractile bands of the SMCs. Maximum peaks corresponding to individual smooth muscle were counted and the number of SMCs per 100 µm length was determined.

Transmission electron microscopy

Brains from adult mice were dissected and fixed by immersion in 5% glutaraldehyde, 4% PFA and 0.1 M sodium cacodylate for 2 weeks at room temperature. Following fixation, brains were washed overnight in 0.1 M sodium cacodylate. Coronal vibratome free-floating sections of 50 µm were collected. The cortices, particularly somatosensory and motor, were microdissected, post-fixed in 1% osmium tetroxide and 1.5% potassium ferrocyanide, dehydrated, and embedded in epoxy resin. Ultrathin sections of 80 nm were then cut from the block surface, collected on copper grids, and counter-stained with Reynold's lead citrate and examined under a 1200EX electron microscope (JEOL) equipped with a 2k CCD digital camera (AMT).

Mean vesicular density

For all transmission electron microscopy quantifications, mean vesicular density values were calculated from the number of vesicles per µm^2 of cell area for each image collected. All images were collected at 12,000× magnification and analysis was performed blinded. Each density value (circle on the graphs) represents an individual vessel (capillary or arteriole). The same colour of the circle represents vessels analysed from the same mouse. Values are expressed as mean ± s.e.m.

Immunohistochemistry

Mice were anaesthetized with ketamine/xylazine via intraperitoneal injection and then mice were transcardially perfused with cold PBS and followed by cold 4% PFA. Brains and retinas were fixed by immersion in 4% PFA/PBS overnight at 4 °C. Next, brains and retinas were washed 3× in PBS. Brain sections were either cut as 50-µm sections on the vibratome or cryopreserved in 30% sucrose, frozen in TissueTek OCT (Sakura) and cut as 25-µm sections on the cryostat. For MFSD2A and eNOS immunohistochemistry, mice were euthanized by cervical dislocation. Brains were snap-frozen with liquid nitrogen and cut as 25-µm sections on the cryostat. Brain sections were fixed with chilled methanol for 10 min. Brain sections and retinas were blocked with 10% goat or donkey serum, 5% BSA, PBST (0.5% Triton X-100) and stained overnight at 4 °C with the following primary antibodies at the indicated concentrations: MFSD2A (1:200, Cell Signaling Technologies; RRID: AB_2617168) or MFSD2A (a gift from D. Silver, as used previously[40]), SMA (1:1,000, Sigma-Aldrich, no. C6198, RRID :AB_476856), ICAM2 (1:200, BD Biosciences, no. 553326, RRID:AB_394784), PECAM (1:200, BD Biosciences, no. 553370; RRID: AB_394816), claudin 5 (Thermo Fisher Scientific, no. 34-1600, RRID:AB_2533157), eNOS (Abcam, no. ab5589; RRID:AB_304967), MYH11 (Abcam, no. ab53219; RRID:AB_2147146) or desmin (ThermoFisher, no. PA1-37556) and TAGLN (Abcam, no. ab14106), followed by corresponding Alexa Fluor-conjugated secondary antibodies (1:500, ThermoFisher) and Alexa Fluor Hydrazide 633 (1:1,000, ThermoFisher). Tissues were mounted with ProLong Gold for imaging.

In situ NO detection

This assay was previously adapted from these studies[41,42]. Mice were deeply anaesthetized with ketamine/xylazine. Mice were transcardially perfused with warm (37 °C) 50 ml PBS, then perfused with 50 ml warm PBS containing 10 µM DAF-2 (Thermo Fisher Scientific, D23842), 100 µM L-arginine and 2 mM $CaCl_2$. Next, mice were perfused with warm PBS again followed by 4% PFA. Brains and kidneys were collected and fixed overnight in 4% PFA at 4 °C. Tissues were sectioned on the vibratome (50 µm) and processed for immunostaining.

Light microscopy

Olympus FluoView FV1200 and Leica SP8 laser scanning confocal microscopes (20×, 0.75 NA, 40×, 1.3 NA, 63× 1.4 NA) and an Olympus VS 120 slide scanner (10×, 0.4 NA) were used for imaging retina flat-mounts and brain sections. Images were processed using Adobe Photoshop, Illustrator, Olympus Fluoview and FIJI (NIH).

Statistical analyses

All statistical analyses were performed using Prism 7 and 8 (GraphPad Software). Two group comparisons were analysed using an unpaired two-tailed Student's *t*-test or non-parametric analyses. Multiple group comparisons were analysed using a one-way ANOVA, followed by a post hoc Bonferroni analysis to correct for multiple comparisons. No data were excluded when performing statistical analysis. The s.e.m. was calculated for all experiments and displayed as errors bars in graphs. Statistical details for specific experiments—including exact *n* values and what *n* represents, precision measures, statistical tests used and definitions of significance—can be found in figure legends. Each colour circle on the graphs throughout the study represents an individual vessel (capillary or arteriole or SMC). The same colour of the circle represents vessels analysed from the same mouse. Values are expressed as mean ± s.e.m. Please see Supplementary Table 1 for statistical test results.

Reporting summary

Further information on research design is available in the Nature Research Reporting Summary linked to this paper.

Data availability

Source Data for quantification described in the text or shown in graphs plotted in Figs. 1–4 and Extended Data Fig. 1–10 are available with the paper.

Code availability

The source code to run the pial arteriolar dilation analysis is available at https://github.com/gulabneuro/Pial-Vasodilation-Analysis. The source code to run the parenchymal arterial dilation analysis is available at https://github.com/gulabneuro/divingArterioleTracking.

31. Pu, W. et al. Mfsd2a^{+} hepatocytes repopulate the liver during injury and regeneration. *Nat. Commun.* **7**, 13369 (2016).
32. Madisen, L. et al. A robust and high-throughput Cre reporting and characterization system for the whole mouse brain. *Nat. Neurosci.* **13**, 133–140 (2010).
33. Madisen, L. et al. A toolbox of Cre-dependent optogenetic transgenic mice for light-induced activation and silencing. *Nat. Neurosci.* **15**, 793–802 (2012).
34. Quina, L. A., Harris, J., Zeng, H. & Turner, E. E. Specific connections of the interpeduncular subnuclei reveal distinct components of the habenulopeduncular pathway. *J. Comp. Neurol.* **525**, 2632–2656 (2017).
35. Chen, T.-W. et al. Ultrasensitive fluorescent proteins for imaging neuronal activity. *Nature* **499**, 295–300 (2013).
36. Shesely, E. G. et al. Elevated blood pressures in mice lacking endothelial nitric oxide synthase. *Proc. Natl Acad. Sci. USA* **93**, 13176–13181 (1996).

37. Raymond, C. S. & Soriano, P. High-efficiency FLP and ΦC31 site-specific recombination in mammalian cells. *PLoS ONE* **2**, e162 (2007).
38. Steger, C. An unbiased detector of curvilinear structures. *IEEE Trans. Pattern Anal. Mach. Intell.* **20**, 113–125 (1998).
39. Chhatbar, P. Y. & Kara, P. Improved blood velocity measurements with a hybrid image filtering and iterative Radon transform algorithm. *Front. Neurosci.* **7**, 106 (2013).
40. Nguyen, L. N. et al. Mfsd2a is a transporter for the essential omega-3 fatty acid docosahexaenoic acid. *Nature* **509**, 503–506 (2014).
41. Kanetsuna, Y. et al. Deficiency of endothelial nitric-oxide synthase confers susceptibility to diabetic nephropathy in nephropathy-resistant inbred mice. *Am. J. Pathol.* **170**, 1473–1484 (2007).
42. Jiang, R. et al. Generation of a conditional allele for the mouse endothelial nitric oxide synthase gene. *Genesis* **50**, 685–692 (2012).

Acknowledgements We thank C. Harvey for his help in the design and construction of the two-photon microscope; O. Mazor and P. Gorelik at the HMS Research Instrumentation Core Facility and T. LaFratta and J. LeBlanc of the Harvard Neuroengineering and Imaging Machine Shop for their help in the construction of the two-photon microscope; S. Ashrafi, J. Cohen, D. Ginty, C. Weitz., G. Yellen and members of the Gu laboratory for comments on the manuscript; C. Lahmann for protocol advice and assistance on cranial window surgery; P. Scherer, R. Adams and B. Zhou for the *Cav1*-floxed, *BMX*^{creER} and *Mfsd2a*^{creER} mice, respectively; D. Silver for the MFSD2A antibody; and the HMS Electron Microscopy Core Facility, HMS Neurobiology Imaging Facility and HMS NeuroDiscovery Center for consultation and instrument availability. This work was supported by Quan Fellowship (B.W.C), NIH T32 and the Mahoney Postdoctoral Fellowship (V.N.), Jane Coffin Childs Fund (A.J.G.), K99 NS102429 (A.J.G), R37 NS046579 (B.L.S.), P30NS072030 (HMS Neurobiology Imaging Facility), the NIH DP1 NS092473 Pioneer Award (C.G.), Fidelity Biosciences Research Initiative (C.G.). The research of C.G. was also supported in part by a Faculty Scholar grant from the Howard Hughes Medical Institute.

Author Contributions B.W.C. and C.G. conceived the project. B.W.C, V.N. and C.G. designed experiments. B.W.C., V.N., A.J.G., K.B. and H.L.Z. performed experiments. B.W.C., V.N., A.J.G., L.K. and P.K. analysed all data. B.W.C. and C.G. wrote the manuscript, with feedback from all authors.

Competing interests The authors declare no competing interests.

Additional information

Supplementary information is available for this paper at https://doi.org/10.1038/s41586-020-2026-1.

Correspondence and requests for materials should be addressed to C.G.

Peer review information *Nature* thanks Dritan Agalliu, Brian MacVicar and the other, anonymous, reviewer(s) for their contribution to the peer review of this work.

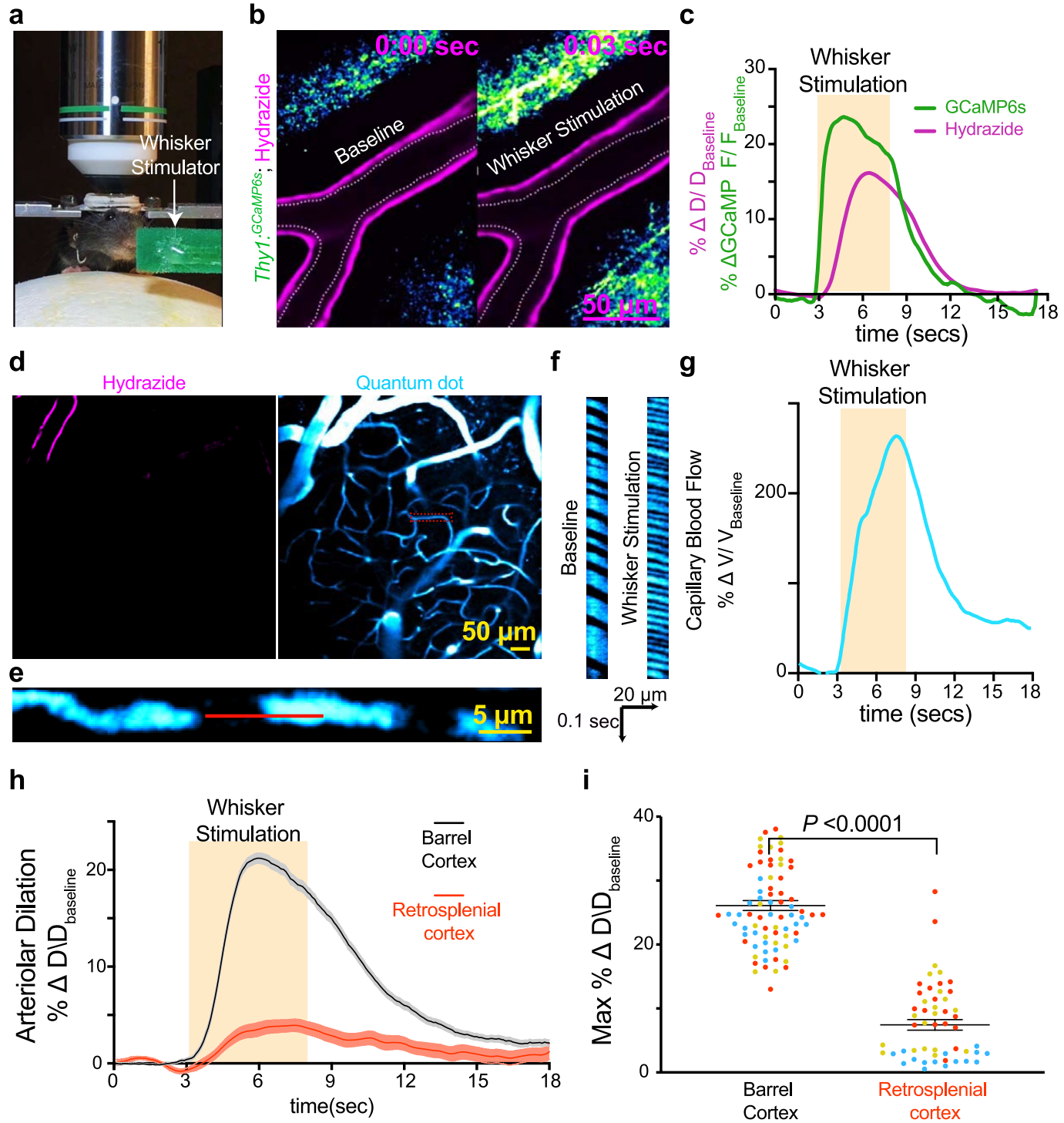

Extended Data Fig. 1 | In vivo two-photon imaging of neurovascular coupling in the barrel cortex and retrosplenial cortex. a, Setup of the in vivo microscopy. Awake mice with cranial windows over the barrel cortex are head-fixed and allowed to move on a foam ball. Whisker stimulator (arrow) is used for brushing whiskers to evoke neural activity in the barrel cortex. **b**–**g**, Imaging in the barrel cortex. **b**, Hydrazide injection in *Thy1*-GCaMP6s mice enables simultaneous imaging of neural activity (green) and arteriolar dilation (magenta). Two-photon imaging of arterioles and neural activity before (left) and after (right) whisker stimulation. Hashes indicate the baseline diameter at time = 0 s. **c**, Time course of change in arteriolar dilation (magenta) and GCaMP6s fluorescence (green). Orange bar signifies the period of whisker stimulation. **d**, Two-photon imaging of arterioles (magenta) and capillary blood flow (blue). After intravenous injection of quantum dots, the plasma is bright whereas the red blood cells are dark. **e**, High magnification of a capillary outlined by the red box in **d**. Minimizing the image size increases the temporal resolution to about 610 Hz or 1.6 ms per frame. **f**, Kymographs of capillary blood flow during baseline (left) and whisker stimulation (right). Kymographs were generated from the parallel line scan (red line) of the capillary blood flow in **e**. **g**, Time course of change in red blood cell velocity. **h**, Time course of change in arteriolar dilation in the barrel cortex (black, $n = 78$ arterioles, 3 mice) and in the retrosplenial cortex (red, $n = 54$ arterioles, 3 mice). **i**, Maximum percentage change in arteriolar dilation upon whisker stimulus in these two brain regions upon whisker stimulus. The orange bar signifies the period of whisker stimulation. Data are mean ± s.e.m.; nested unpaired, two-tailed *t*-test for **i**.

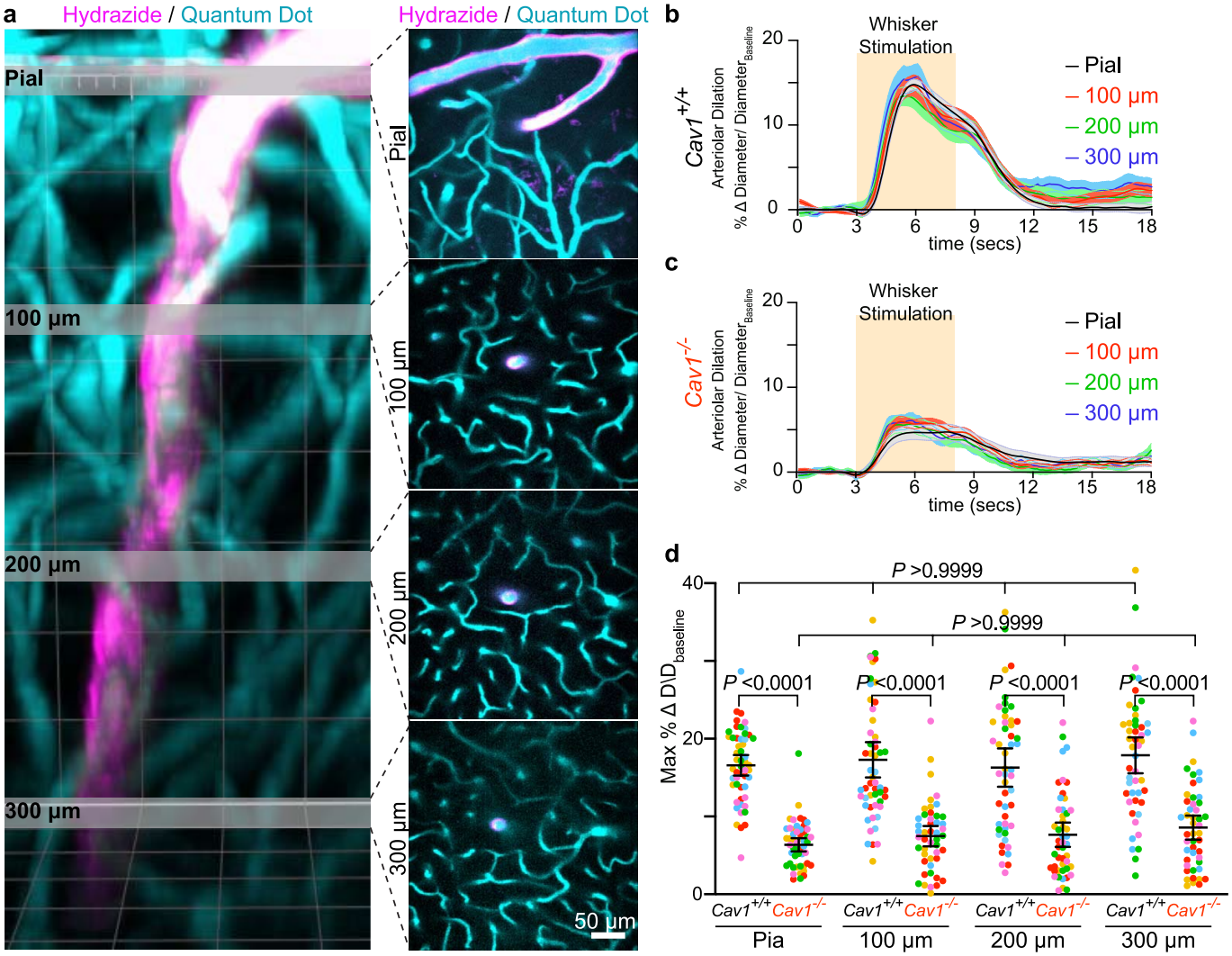

Extended Data Fig. 2 | *Cav1*-knockout mice have impaired vasodilation in both pial arteries and penetrating arterioles diving deep into the parenchyma. a, Three-dimensional volume rendering of a two-photon-imaged site in *Cav1*$^{+/+}$ mouse barrel cortex, from the pial surface to a depth of about 400 µm. The lumen of all vessels is filled with quantum dots (blue) and arterioles are labelled with hydrazide (magenta). The deepest imaged bin is at 300 µm because we see the appearance of the hydrazide start at 300 µm, indicating that this is at the start of the arteriolar vessels. This observation is also consistent with a previous study[5], which characterized hydrazide as an arteriolar vessel marker. Grey slices correspond to *z* cross-sections shown per depth. Independent replicates for **a** were performed in five wild-type mice. **b**, **c**, Time course of change in arteriolar dilation in the barrel cortex from *Cav1*$^{+/+}$ ($n = 5$ mice, 10–15 arterioles per depth) (**b**) and *Cav1*$^{-/-}$ mice ($n = 5$ mice, 10–15 arterioles per depth) (**c**). **d**, Maximum percentage change in arteriolar dilation upon whisker stimulation between in *Cav1*$^{+/+}$ and *Cav1*$^{-/-}$ mice at the indicated depth. Statistical significance was determined by two-way ANOVA with a post hoc Bonferroni multiple comparison adjustment for **d**. All data are mean ± s.e.m. We compared the maximum percentage change in arteriolar dilation upon whisker stimulation between *Cav1*$^{+/+}$ and *Cav1*$^{-/-}$ mice at each depth and also compared the responses across depth within the same genotype.

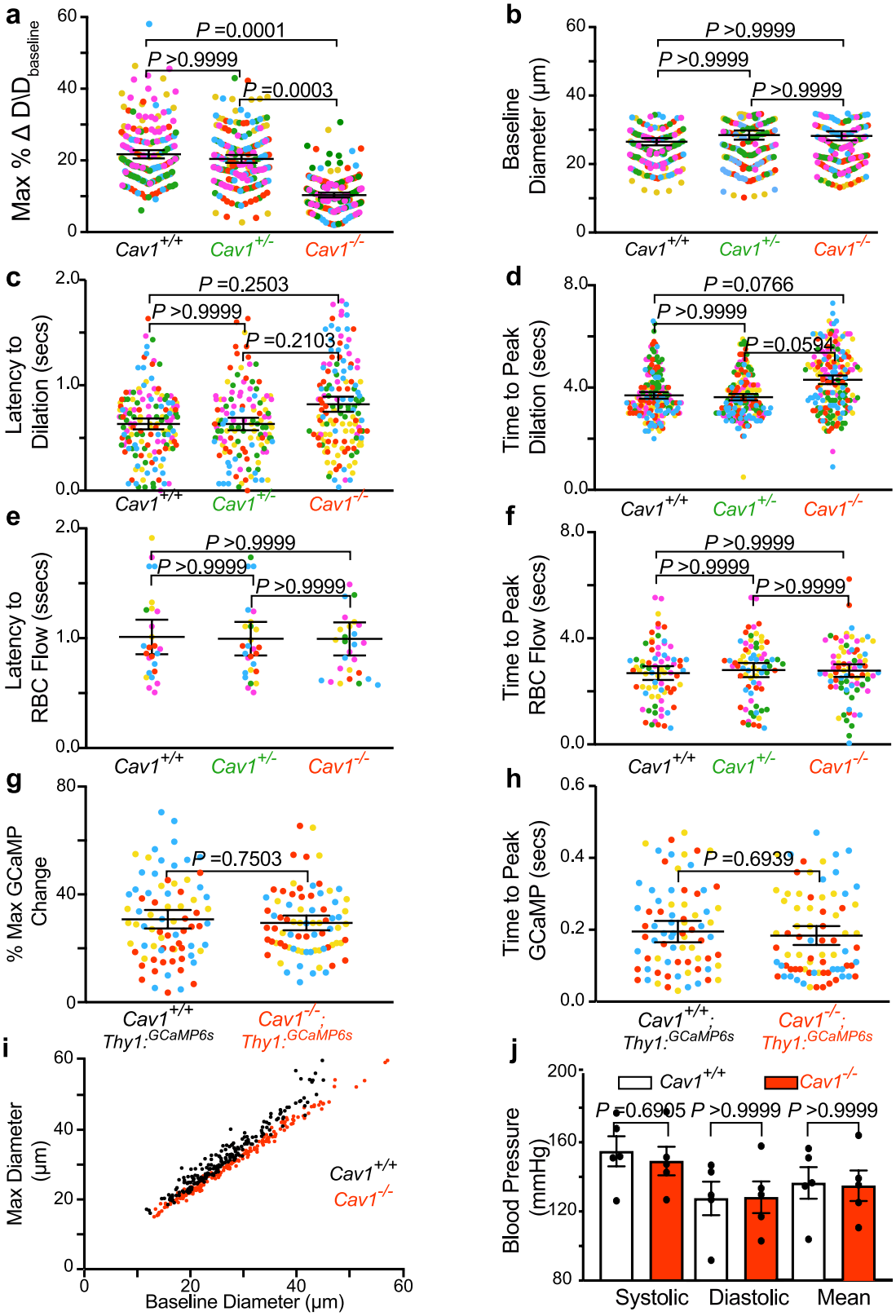

Extended Data Fig. 3 | See next page for caption.

Extended Data Fig. 3 | *Cav1*- knockout mice have attenuated vasodilation but normal neural activity and neurovascular coupling kinetics. a–**d**, Maximum percentage change in dilation response (**a**) and baseline diameter (**b**) latency to maximum change in arteriolar dilation (**c**), time to peak dilation (**d**) in $Cav1^{+/+}$ ($n = 193$ arterioles, 40 capillaries, 5 mice), $Cav1^{+/-}$ ($n = 123$ arterioles, 40 capillaries, 5 mice), and $Cav1^{-/-}$ mice ($n = 153$ arterioles, 31 capillaries, 5 mice). **e**, **f**, Latency to maximum red blood cell flow velocity (**e**) and time to peak red blood cell flow (**f**) in $Cav1^{+/+}$ ($n = 193$ arterioles, 40 capillaries, 5 mice), $Cav1^{+/-}$ ($n = 123$ arterioles, 40 capillaries, 5 mice) and $Cav1^{-/-}$ mice ($n = 153$ arterioles, 31 capillaries, 5 mice). **g**, **h**, Maximum percentage change in GCaMP6s (**g**) and latency to peak change in GCaMPs (**h**) in $Cav1^{+/+}$;*Thy1*-GCaMP6s ($n = 78$ field of views of the neuropils, 5 mice) and $Cav1^{-/-}$;*Thy1*-GCaMP6s ($n = 78$ neuropils, 5 mice). Each circle represents an individual trial of GCaMP6s signal. **i**, Baseline diameter to absolute maximum diameter response during whisker stimulation in $Cav1^{+/+}$ and $Cav1^{-/-}$ mice. **j**, Tail-cuff blood pressure measurements between $Cav1^{+/+}$ ($n = 5$ mice) and $Cav1^{-/-}$ mice ($n = 5$ mice). Statistical significance was determined by a one-way nested ANOVA with a post hoc Bonferroni multiple comparison adjustment for **a**–**f**, a nested unpaired, two-tailed *t*-test for **g**, **h**, and two-tailed Mann–Whitney *U* test for **j**. All data are mean ± s.e.m.

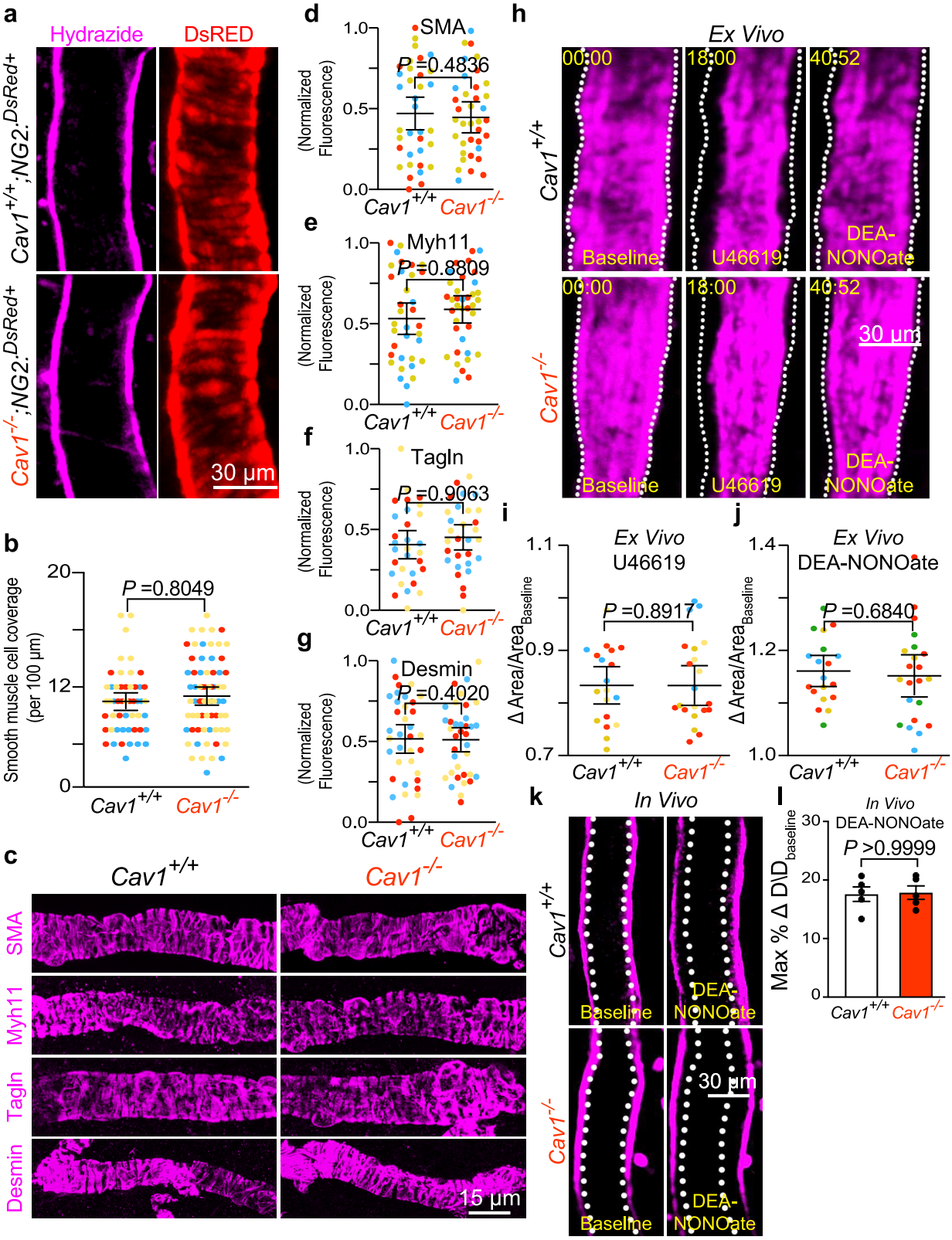

Extended Data Fig. 4 | See next page for caption.

Extended Data Fig. 4 | *Cav1*-mutant mice exhibit normal SMC integrity and function. a, In vivo two-photon microscopy images of hydrazide (magenta) and DsRed (red) from *Cav1*$^{+/+}$*NG2*$^{DsRED+}$ and *Cav1*$^{-/-}$*NG2*$^{DsRED+}$ mice. **b**, Quantification of DsRED^{+} SMCs per 100 µm as shown in **a**, in *Cav1*$^{+/+}$ ($n = 3$ mice, 27 arterioles) and *Cav1*$^{-/-}$ ($n = 3$ mice, 28 arterioles) mice. **c**, Immunostaining for SMC contractile proteins, including SMA, MYH11, TAGLN and desmin on brain arterioles from *Cav1*$^{+/+}$ and *Cav1*$^{-/-}$ mice. **d**–**g**, Normalized fluorescence quantification of the various contractile proteins from *Cav1*$^{+/+}$ and *Cav1*$^{-/-}$ mice. **h**, Still frame images of arterioles labelled with hydrazide (magenta) in ex vivo acute brain slices from *Cav1*$^{+/+}$ and *Cav1*$^{-/-}$ mice using two-photon microscopy. Left, arterioles during baseline; middle, arterioles during U46619 (thromboxane agonist) treatment; right, arterioles during DEA NONOate (NO donor) treatment. White hashes outline the arterioles during baseline based on time = 0 min. **i**, **j**, Maximum arteriolar contraction by U46619 (**i**) and maximum arteriolar dilation by DEA NONOate (**j**) on acute brain slices from *Cav1*$^{+/+}$ ($n = 5$ mice, 19 arterioles) and *Cav1*$^{-/-}$ ($n = 5$ mice, 22 arterioles). **k**, In vivo images of arterioles labelled with hydrazide (magenta) from *Cav1*$^{+/+}$ and *Cav1*$^{-/-}$ mice using two-photon microscopy. Left, arterioles during baseline; right, arterioles during DEA NONOate superfusion. White hashes outline the arterioles during baseline based on time = 0 s. **l**, Quantification of maximum arteriolar dilation during DEA NONOate superfusion in vivo ($n = 5$ mice for both genotypes). Statistical significance was determined by nested, unpaired, two-tailed *t*-test for **b**, **d**–**g**, **i**, **j**, and by two-tailed Mann–Whitney *U* test for **l**. Data shown as mean ± s.e.m.

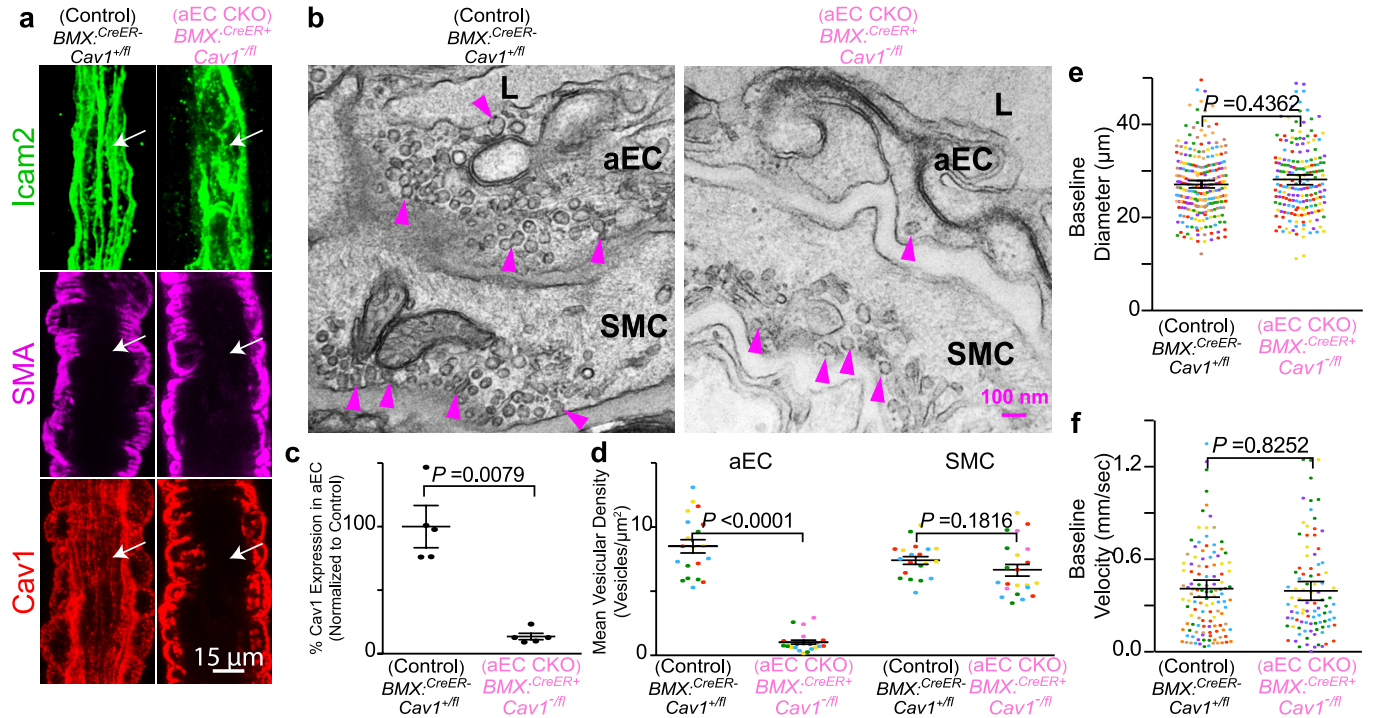

Extended Data Fig. 5 | Caveolae in CNS aECs are abolished in aEC conditional *Cav1*-knockout mice. a, Immunostaining of adult brain sections for ECs (ICAM2, green), SMCs (SMA, magenta) and CAV1 (red) from control (BMX^{creER-};$Cav1^{+/fl}$) and aEC-specific conditional CAV1 mutant (BMX^{creER+};$Cav1^{-/fl}$) mice. Arrows point to aECs. **b**, Transmission electron microscopy images of CNS aECs and SMCs from control and aEC-specific conditional *Cav1*-mutant mice. Arrowheads point to caveolae. L, Lumen. **c**, Quantification of mean normalized immunofluorescence of CAV1 in aECs from control ($n = 5$ mice) and aEC-specific conditional *Cav1*-mutant mice ($n = 5$ mice). **d**, Quantification of the mean vesicular density in aECs and SMCs between control ($n = 4$ mice, 20 arterioles) and aEC-specific conditional *Cav1*-mutant mice ($n = 5$ mice, 22 arterioles). **e**, **f**, Quantification of baseline diameter (**e**) and baseline velocity in control (BMX^{creER-};$Cav1^{+/fl}$; $n = 7$ mice, 260 arterioles, 122 capillaries) and aEC conditional *Cav1*-knockout mice (BMX^{creER+};$Cav1^{-/fl}$; $n = 5$ mice, 193 arterioles, 94 capillaries). Statistical significance was determined by Mann–Whitney test for (**c**) and nested, unpaired, two-tailed *t*-test for (**d**–**f**). Data are shown as mean ± s.e.m.

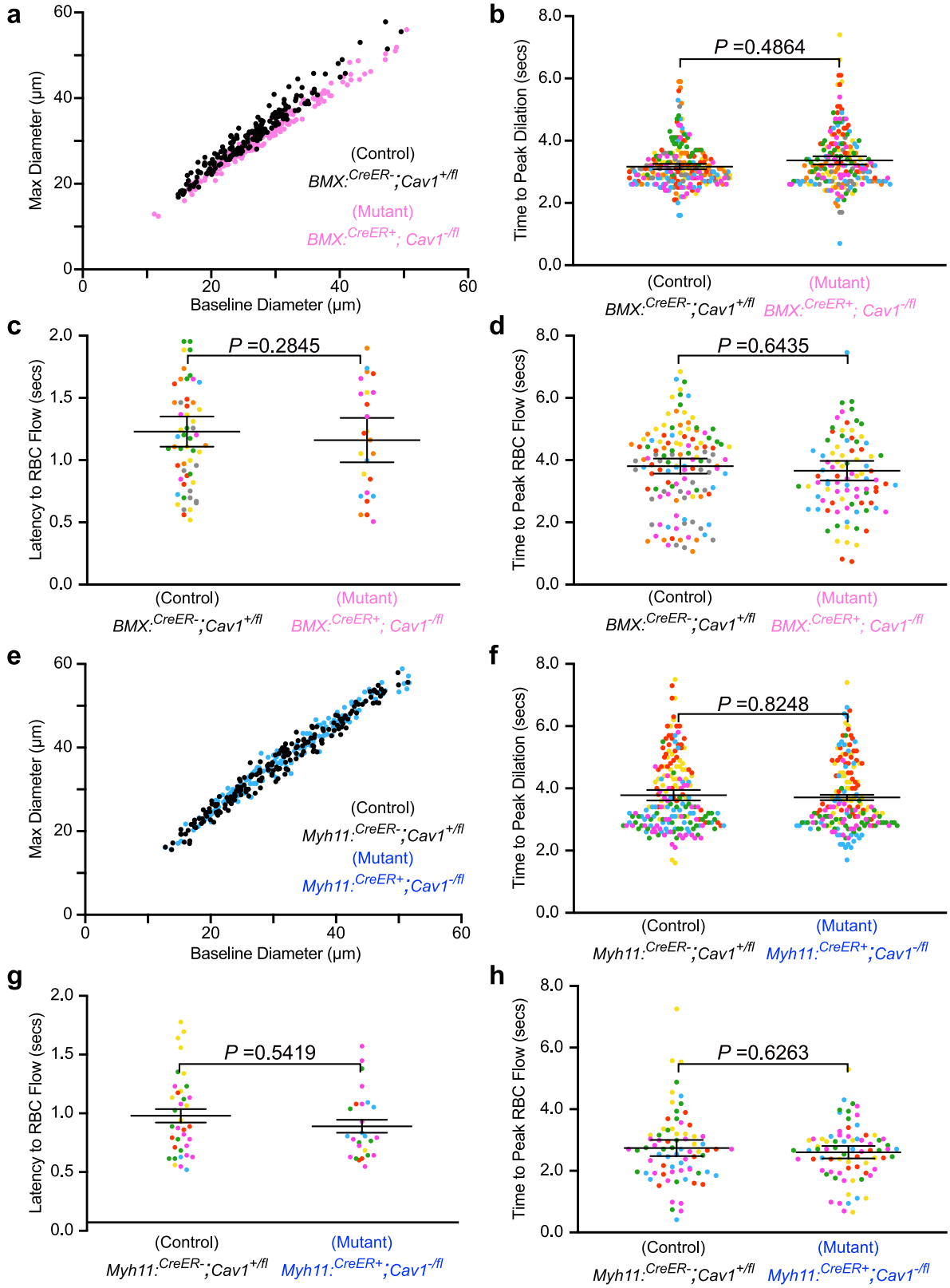

Extended Data Fig. 6 | See next page for caption.

Extended Data Fig. 6 | Conditional aEC-specific and SMC *Cav1*-knockout mice have normal neurovascular coupling kinetics. a, Baseline diameter to absolute maximum diameter response during whisker stimulation in control (BMX^{creER-};$Cav1^{+/fl}$) and mutant (BMX^{creER+};$Cav1^{-/fl}$) mice. **b**, Quantification of time to peak arteriolar dilation in control (BMX^{creER-};$Cav1^{+/fl}$; $n = 7$ mice, 234 arterioles) and aEC-specific conditional *Cav1*-mutant (BMX^{creER+};$Cav1^{-/fl}$; $n = 5$ mice; 202 arterioles) mice. **c**, Quantification of latency to peak red blood cell flow velocity in control (BMX^{creER-};$Cav1^{+/fl}$; $n = 7$ mice; 58 capillaries) and aEC-specific conditional *Cav1*-mutant (BMX^{creER+};$Cav1^{-/fl}$; $n = 5$ mice; 25 capillaries) mice. **d**, Quantification of time to peak red blood cell flow velocity in control (BMX^{creER-};$Cav1^{+/fl}$; $n = 7$ mice; 127 capillaries) and aEC-specific conditional *Cav1*-mutant (BMX^{creER+};$Cav1^{-/fl}$; $n = 5$ mice; 94 capillaries) mice. **e**, Baseline diameter to absolute maximum diameter response during whisker stimulation in control ($Myh11^{creER-}$;$Cav1^{+/fl}$) and mutant ($Myh11^{creER+}$;$Cav1^{-/fl}$ mice. **f**, Quantification of time to peak arteriolar dilation in control ($Myh11^{creER-}$;$Cav1^{+/fl}$; $n = 5$ mice, 193 arterioles) and SMC conditional *Cav1*-mutant ($Myh11^{creER+}$;$Cav1^{-/fl}$; $n = 5$ mice; 180 arterioles) mice. **g**, Quantification of latency to red blood cell flow in control ($Myh11^{creER-}$;$Cav1^{+/fl}$; $n = 5$ mice; 36 capillaries) and SMC conditional *Cav1*-mutant ($Myh11^{creER+}$;$Cav1^{-/fl}$; $n = 5$ mice; 26 capillaries) mice. **h**, Quantification time to peak red blood cell flow velocity in ($Myh11^{creER-}$;$Cav1^{+/fl}$; $n = 5$ mice; 75 capillaries) and SMC conditional *Cav1*-mutant ($Myh11^{creER+}$;$Cav1^{-/fl}$; $n = 5$ mice; 75 capillaries) mice. Statistical significance was determined by a nested unpaired, two-tailed *t*-test for **b**–**d**, **f**–**h**).

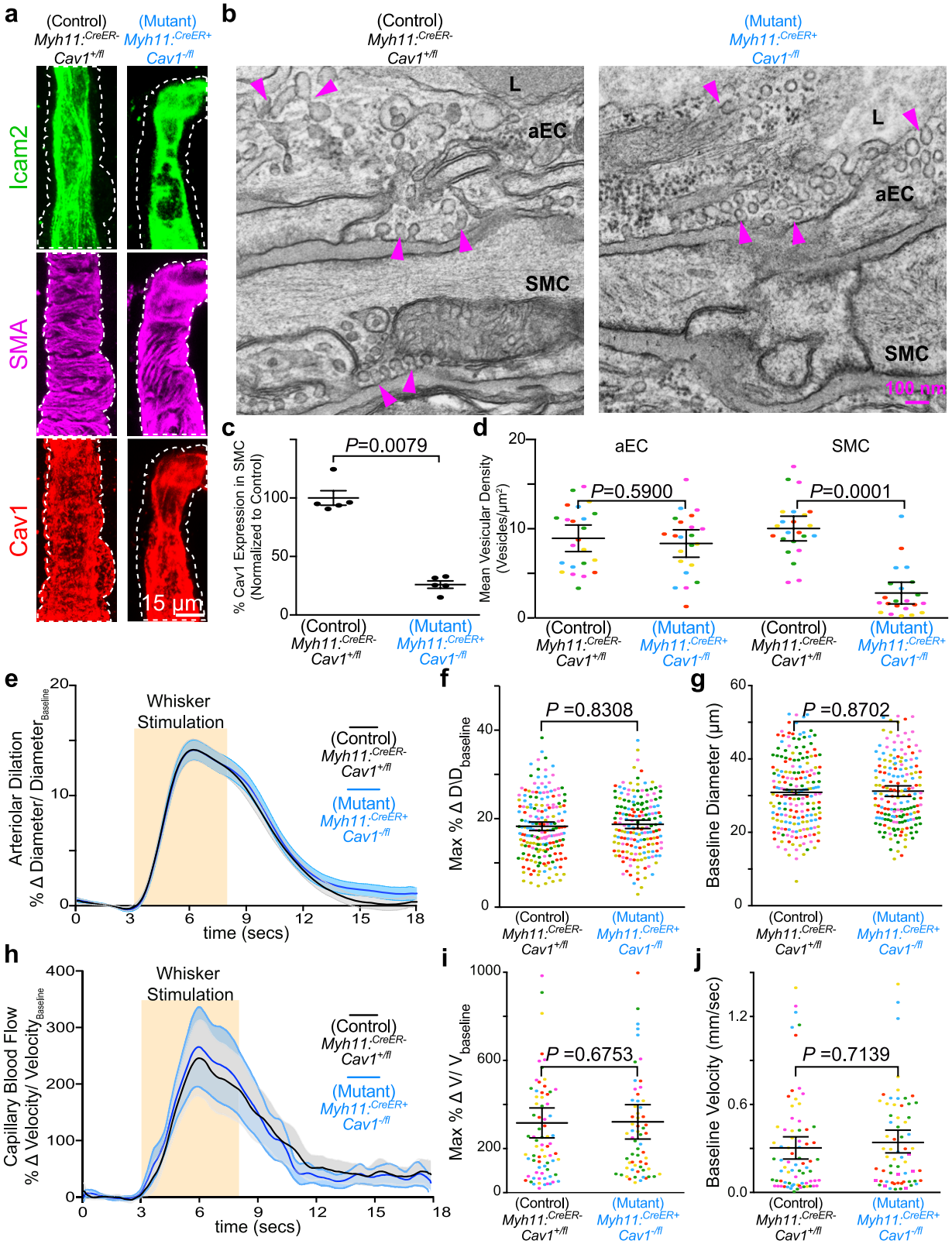

Extended Data Fig. 7 | See next page for caption.

Extended Data Fig. 7 | Conditional SMC-specific *Cav1*-knockout mice have normal neurovascular coupling. a, Immunostaining on brain sections for ECs (ICAM2, green), SMCs (SMA, magenta) and CAV1 (red) from control and SMC conditional *Cav1*-mutant mice. **b**, Transmission electron microscopy images of CNS aECs and SMCs from control and SMC conditional *Cav1*-mutant mice. Arrowheads point to caveolae. L, Lumen. **c**, Mean normalized immunofluorescence of CAV1 in SMCs from control ($n = 5$ mice) and SMC-specific conditional *Cav1*-mutant mice ($n = 5$ mice). **d**, Quantification of the mean vesicular density in aECs and SMCs in control ($n = 5$ mice, 23 arterioles) and SMC conditional $Cav1^{-/-}$ mice ($n = 5$ mice, 22 arterioles). **e**–**g**, Time course of change in arteriolar dilation (**e**), maximum percentage change in arteriolar dilation (**f**) and baseline diameter (**g**) in control ($n = 7$ mice, 193 arterioles) and SMC conditional *Cav1*-mutant mice ($n = 5$ mice, 176 arterioles). **h**–**j**, Time course of change in red blood cell velocity (**h**), maximum percentage change in red blood cell velocity (**i**) and baseline velocity (**j**) in control ($n = 7$ mice, 75 capillaries) and SMC conditional *Cav1*-mutant mice ($n = 5$ mice, 64 capillaries). Statistical significance was determined by unpaired, two-tailed Mann–Whitney *U* test for **c** and a nested, unpaired, two-tailed *t*-test for (**d**, **f**, **g**, **i**, **j**). Data are mean ± s.e.m.

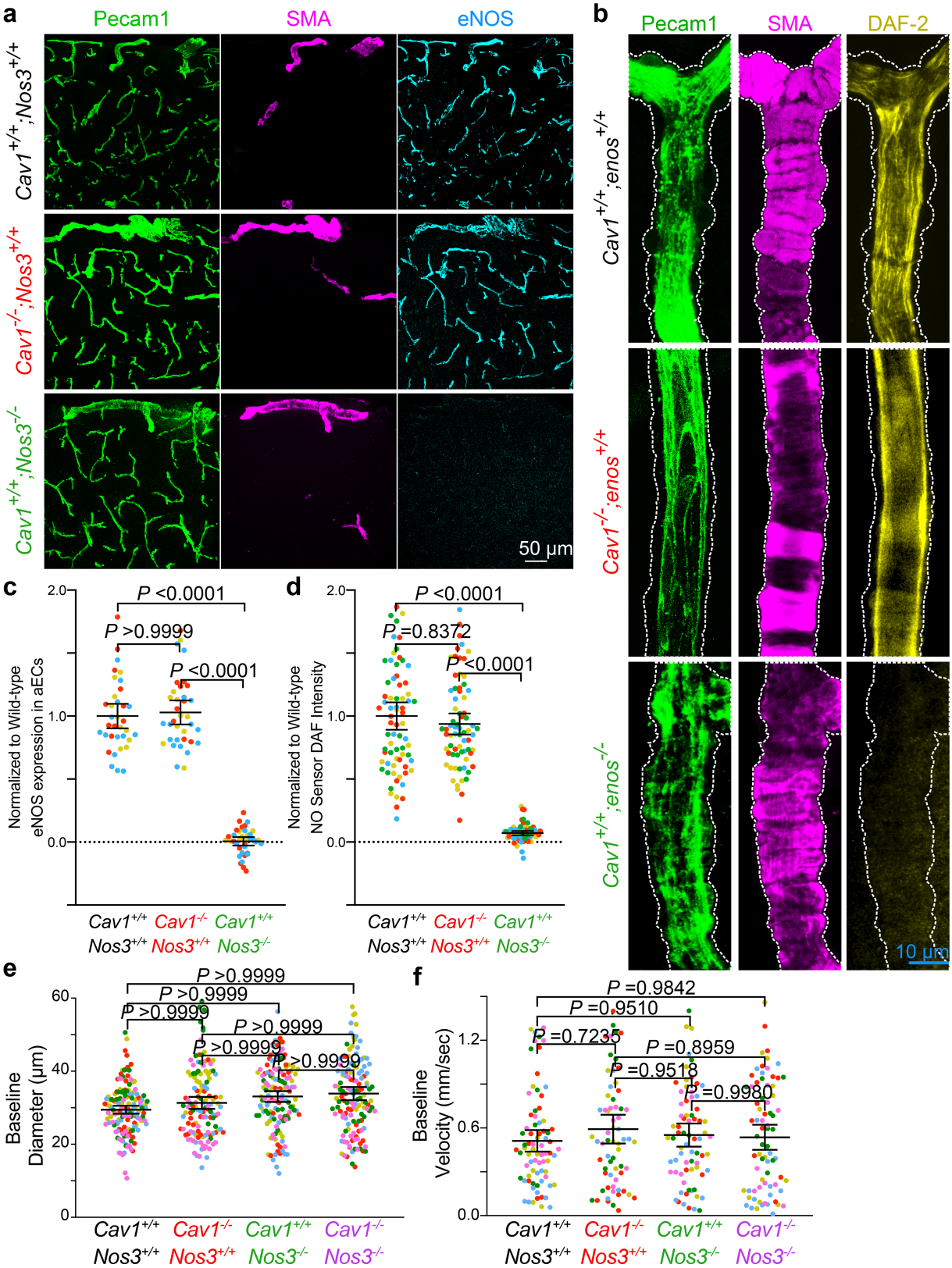

Extended Data Fig. 8 | See next page for caption.

Extended Data Fig. 8 | *Cav1*-mutant mice have normal levels of eNOS protein and NO in CNS aECs and *Cav1* and *Nos3* double knockout mice have normal baseline diameter and red blood cell flow. a, Immunostaining on adult brain sections for ECs (PECAM1, green), arterioles (SMA, magenta) and eNOS (cyan) from *Cav1*$^{+/+}$*Nos3*$^{+/+}$, *Cav1*$^{-/-}$*Nos3*$^{+/+}$ and *Cav1*$^{+/+}$*Nos3*$^{-/-}$ mice. Independent replications were performed on three mice per genotype. **b**, Immunostaining for (PECAM1, green) and arterioles (SMA, magenta) on brain sections from *Cav1*$^{+/+}$*Nos3*$^{+/+}$, *Cav1*$^{-/-}$*Nos3*$^{+/+}$ and *Cav1*$^{+/+}$*Nos3*$^{-/-}$ mice after in vivo perfusion of NO-sensitive dye; DAF-2, yellow. Independent replicates were performed on four mice per genotype. **c**, Quantification of eNOS immunofluorescence intensity as shown in **a** in aECs from *Cav1*$^{+/+}$*Nos3*$^{+/+}$ (n = 3 mice, 35 images), *Cav1*$^{-/-}$*Nos3*$^{+/+}$ (n = 3 mice, 35 images) and *Cav1*$^{+/+}$*Nos3*$^{-/-}$ (n = 3 mice, 37 images). **d**, Quantification of DAF-2 intensity in aECs as shown in (**b**) from *Cav1*$^{+/+}$*Nos3*$^{+/+}$ (n = 4 mice, 73 images), *Cav1*$^{-/-}$*Nos3*$^{+/+}$ (n = 4 mice, 71 images), and *Cav1*$^{+/+}$*Nos3*$^{-/-}$ (n = 4 mice, 64 images). **e**, **f**, Quantification of baseline diameter (**e**) and baseline velocity (**f**) in *Cav1*$^{+/+}$*Nos3*$^{+/+}$ (n = 5 mice, 148 arterioles, 76 capillaries), *Cav1*$^{-/-}$*Nos3*$^{+/+}$ (n = 5 mice, 128 arterioles, 68 capillaries), *Cav1*$^{+/+}$*Nos3*$^{-/-}$ (n = 5 mice, 137 arterioles, 73 capillaries) and *Cav1*$^{-/-}$*Nos3*$^{-/-}$ mice (n = 5 mice, 139 arterioles, 74 capillaries). Statistical significance was determined by nested, unpaired, two-tailed t-test for **c**, **d**, and nested, one-way ANOVA with a post hoc Bonferroni multiple-comparison adjustment for **e**, **f**. Data are mean ± s.e.m.

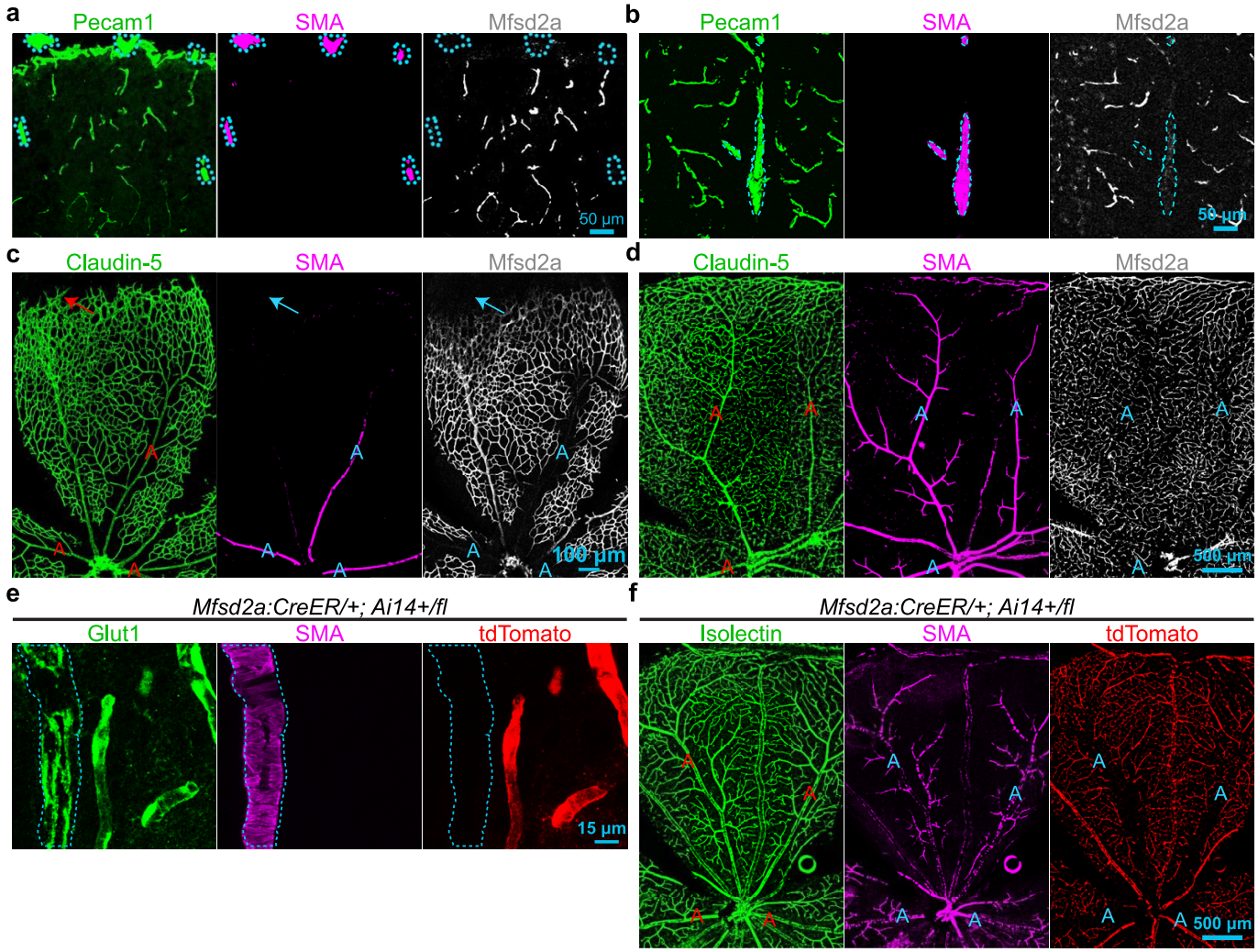

Extended Data Fig. 9 | MFSD2A is not detected in CNS arterioles in brain and retina. a, **b**, Immunostaining on postnatal day (P)5 (**a**) and adult (**b**) brain sections for ECs (PECAM1, green), SMCs (SMA, magenta) and MFSD2A (white) from wild-type mice. Blue hashes outline SMA$^+$ arterioles. **c**, **d**, Immunostaining on P5 (**c**) and adult (**d**) retina for ECs (claudin 5, green), SMCs (SMA, magenta) and MFSD2A (white) from wild-type mice. A, arterioles. MFSD2A is absent in nascent, distal vessel (arrows) in P5 retina in **c**. **e**, **f**, Tamoxifen-treated, adult knock-in *Mfsd2a*$^{creER+}$;*Ai14*$^{+/fl}$ reporter mice demonstrates that tdTomato is absent in SMA$^+$ arterioles but present in SMA$^-$ capillaries in brain (**e**) and retina (**f**). Blue hashes and A indicate SMA$^+$ arterioles. Independent replicates for **a**–**f** were performed on five wild-type mice.

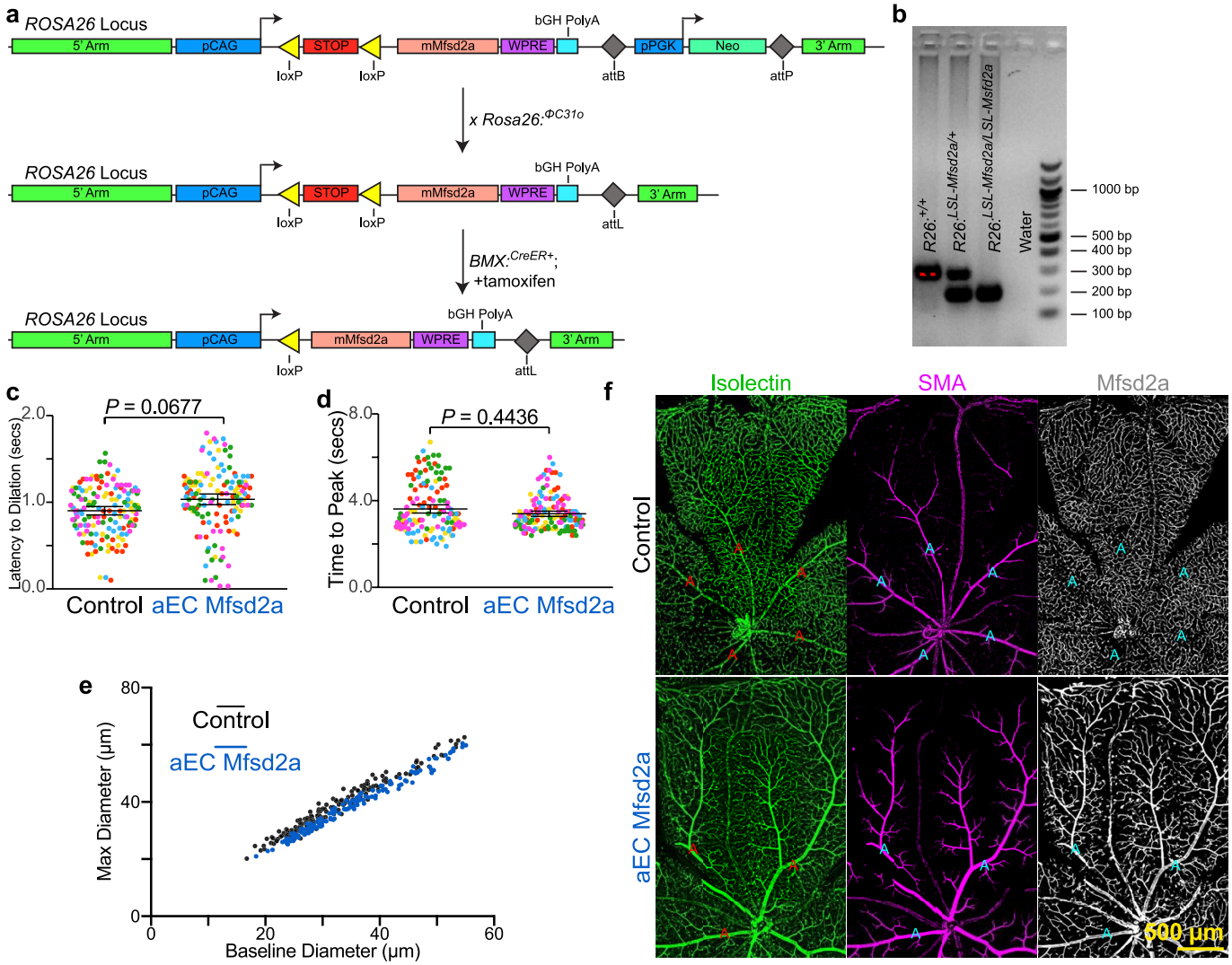

Extended Data Fig. 10 | Generation of a Cre-dependent MFSD2A-overexpression transgenic mouse (*R26*$^{LSL\text{-}Mfsd2a}$). **a**, Construct for Cre-dependent MFSD2A overexpression knocked-in to the ROSA26 locus. Mating with *ROSA26:ΦC31* recombinase mice removes the neomycin selection cassette. Subsequent mating with *BMX*^{creER} and tamoxifen injection enables ectopic overexpression of *Mfsd2a* in aECs. **b**, PCR genotyping of Cre-dependent MFSD2A-overexpression mice. **c**, Quantification of latency to changes in arteriolar dilation in control (*BMX*$^{creER-}$;*R26*$^{LSL\text{-}Mfsd2a/+}$; $n = 5$ mice, 149 arterioles) and aEC-specific MFSD2A overexpression (*BMX*$^{creER+}$;*R26*$^{LSL\text{-}Mfsd2a/+}$; $n = 5$ mice; 138 arterioles) mice. **d**, Quantification of time to peak arteriolar dilation in control (*BMX*$^{creER-}$;*R26*$^{LSL\text{-}Mfsd2a/+}$; $n = 5$ mice, 149 arterioles) and aEC-specific conditional *Cav1*-mutant (*BMX*$^{creER+}$;*R26*$^{LSL\text{-}Mfsd2a/+}$; $n = 5$ mice, 138 arterioles) mice. **e**, Baseline diameter to absolute maximum diameter response during whisker stimulation in control (*BMX*$^{creER-}$;*R26*$^{LSL\text{-}Mfsd2a/+}$; $n = 5$ mice, 149 arterioles) and aEC-specific conditional *Cav1*-mutant (*BMX*$^{creER+}$;*R26*$^{LSL\text{-}Mfsd2a/+}$; $n = 5$ mice; 138 arterioles) mice. **f**, Immunostaining on adult retinas for ECs (isolectin, green), SMCs (SMA, magenta) and MFSD2A (white) from control and aEC-specific MFSD2A-overexpression mice. Independent replications for **f** were performed on three mice per genotype. Statistical significance was determined by a nested unpaired, two-tailed *t*-test for **c**, **d**.

nature research

Corresponding author(s): Chenghua Gu

Last updated by author(s): 02-18-2019

Reporting Summary

Nature Research wishes to improve the reproducibility of the work that we publish. This form provides structure for consistency and transparency in reporting. For further information on Nature Research policies, see Authors & Referees and the Editorial Policy Checklist.

Statistics

For all statistical analyses, confirm that the following items are present in the figure legend, table legend, main text, or Methods section.

n/a	Confirmed	
☐	☒	The exact sample size (*n*) for each experimental group/condition, given as a discrete number and unit of measurement
☐	☒	A statement on whether measurements were taken from distinct samples or whether the same sample was measured repeatedly
☐	☒	The statistical test(s) used AND whether they are one- or two-sided *Only common tests should be described solely by name; describe more complex techniques in the Methods section.*
☒	☐	A description of all covariates tested
☐	☒	A description of any assumptions or corrections, such as tests of normality and adjustment for multiple comparisons
☐	☒	A full description of the statistical parameters including central tendency (e.g. means) or other basic estimates (e.g. regression coefficient) AND variation (e.g. standard deviation) or associated estimates of uncertainty (e.g. confidence intervals)
☐	☒	For null hypothesis testing, the test statistic (e.g. *F*, *t*, *r*) with confidence intervals, effect sizes, degrees of freedom and *P* value noted *Give P values as exact values whenever suitable.*
☒	☐	For Bayesian analysis, information on the choice of priors and Markov chain Monte Carlo settings
☐	☒	For hierarchical and complex designs, identification of the appropriate level for tests and full reporting of outcomes
☒	☐	Estimates of effect sizes (e.g. Cohen's *d*, Pearson's *r*), indicating how they were calculated

Our web collection on statistics for biologists contains articles on many of the points above.

Software and code

Policy information about availability of computer code

Data collection	The following softwares were used to collect the data in this study: • ScanImage 5.1 for two-photon imaging (Vidrio Technologies) • LAS X 3.0.16120.2 for Leica SP8 Confocal Imaging • OlyVIA Ver.2.9.1 for VS120 Virtual Slide Microscope
Data analysis	• Graphpad Prism 7 and 8 • MATLAB R2018b; Script for Pial and deep Arteriolar Dilation analysis is available as listed on "Code Availability" • Microsoft Excel 2016 • Adobe Photoshop CS6 • NIH ImageJ 2.0.0 • Geneious 10.0.09

For manuscripts utilizing custom algorithms or software that are central to the research but not yet described in published literature, software must be made available to editors/reviewers. We strongly encourage code deposition in a community repository (e.g. GitHub). See the Nature Research guidelines for submitting code & software for further information.

Data

Policy information about availability of data

All manuscripts must include a data availability statement. This statement should provide the following information, where applicable:

- Accession codes, unique identifiers, or web links for publicly available datasets
- A list of figures that have associated raw data
- A description of any restrictions on data availability

Data for quantification mentioned in text or shown in graphs plotted in Figs. 1-4 and Extended Fig. 1-10 will be available in the online version of this paper at www.nature.com/nature. Custom MATLAB scripts and ImageJ macros used to generate and analyzed datasets in this study are available at: MATLAB script to

analyze blood flow is available from Pratik Y. Chhatbar and Prakash Kara et al. (2013).

Field-specific reporting

Please select the one below that is the best fit for your research. If you are not sure, read the appropriate sections before making your selection.

☒ Life sciences ☐ Behavioural & social sciences ☐ Ecological, evolutionary & environmental sciences

For a reference copy of the document with all sections, see nature.com/documents/nr-reporting-summary-flat.pdf

Life sciences study design

All studies must disclose on these points even when the disclosure is negative.

Sample size	For in vivo two photon, confocal and electron microscopy data, we performed preliminary experiments to identify the variation. We then perform a power test to identify appropriate sample sizes of images/videos per mouse. Based on previous experience with similar studies, the sample sizes were sufficient.
Data exclusions	In vivo two photon videos were excluded when the quality of the videos was too poor for data analysis. Variations in recovery from the craniotomy, in rare instances, affected the cranial window quality causing low signal to noise. Signal to noise ratio was used as a criterion for excluding two-photon data.
Replication	The experimental findings reported where verified as reproducible through the collection of multiple technical replicates and mice. When possible, the data was collected and analyzed blindly to genotype.
Randomization	Mice were randomized based on their genotypes and allocated randomly in the their respective genotype group. Field of views were randomly sampled.
Blinding	Acquisition, collection and analysis of the experiments were performed all blinded to the genotypes and performed by independent people. Only after the data was completely analyzed were the genotypes unblinded.

Reporting for specific materials, systems and methods

We require information from authors about some types of materials, experimental systems and methods used in many studies. Here, indicate whether each material, system or method listed is relevant to your study. If you are not sure if a list item applies to your research, read the appropriate section before selecting a response.

Materials & experimental systems

n/a	Involved in the study
☐	☒ Antibodies
☒	☐ Eukaryotic cell lines
☒	☐ Palaeontology
☐	☒ Animals and other organisms
☒	☐ Human research participants
☒	☐ Clinical data

Methods

n/a	Involved in the study
☒	☐ ChIP-seq
☒	☐ Flow cytometry
☒	☐ MRI-based neuroimaging

Antibodies

Antibodies used	α-Mfsd2a (1:200, Cell Signaling Technologies; RRID: AB_2617168) α-Mfsd2a (generous gift from Dr. David Silver as used previously) α-SMA (1:1000, Sigma-Aldrich Cat# C6198, RRID:AB_476856; Clone name:1A4; lot no.: 058M4761V) α-ICAM2 (1:200, BD Biosciences Cat# 553326, RRID:AB_394784; Clone 3C4(mIC2/4); lot no.: 8248688) α-PECAM (R and D Systems Cat# AF3628, RRID:AB_2161028) α-Claudin-5 (Thermo Fisher Scientific Cat# 34-1600, RRID:AB_2533157, lot no.:TJ276183) α-eNOS (Abcam Cat# ab5589, RRID:AB_304967) α-Cav1 (Cell Signaling Technology Cat# 3267, RRID:AB_2275453, Clone D46G3) α-Glut1 (Millipore Cat# 07-1401, RRID:AB_1587074; lot 3021918) α-CNN1 (Abcam Cat# ab46794, RRID:AB_2291941, Clone EP798Y) α-Desmin (Thermo Fisher Scientific Cat# PA1-37556, RRID:AB_2292917; lot no.: QI2081282) α-Tagln (Abcam Cat# ab14106, RRID:AB_443021) α-Myh11 (Abcam Cat# ab53219, RRID:AB_2147146; lot no.: GR3261273-2)
Validation	α-Mfsd2a (Cell Signaling) has been validated using immunohistochemistry on Mfsd2a brain KO tissue as previously demonstrated in Ben-Zvi et al. Nature 2014 α-Mfsd2a (Gift from David Silver) has been validated using immunohistochemistry on Mfsd2a brain KO tissue as previously

demonstrated in Nyguen et al. Nature 2014.
α-SMA is valid using immunohistochemistry because staining was specifically localized to smooth muscle cells on arteries.
α-ICAM2 is valid using immunohistochemistry because the staining is consistent with the known expression of endothelial cells and manufacturer routinely test by flow cytometry.
α-PECAM is valid using immunohistochemistry because the staining is consistent with the known expression of endothelial cells and extensively used in many publications.
α-Claudin-5 is valid using immunohistochemistry because the staining is consistent with the known expression of CNS endothelial cells and extensively used in many publications
α-eNOS is valid using immunohistochemistry because antibody has been validated on eNOS knockout tissue on brain and expression is consistent with endothelial cells
α-Cav1is valid using immunohistochemistry because antibody has been validated on Cav1 knockout tissue as previously validated on Andreone et al. 2017. Neuron
α-Glut1 is valid using immunohistochemistry because the staining is consistent with the known expression of CNS endothelial cells
α-CNN1 is valid using immunohistochemistry because staining was specifically localized to smooth muscle cells on arteries and used previously by (Vanlandewijck et al., 2018).
α-Desmin is valid using immunohistochemistry because the staining is consistent with the known expression of mural cells.
α-Tagln is valid because staining was specifically localized to smooth muscle cells on arteries and used previously by (Vanlandewijck et al., 2018).
α-Myh11 is valid using immunohistochemistry because staining was specifically localized to smooth muscle cells on arteries and used previously by (Vanlandewijck et al., 2018).

Animals and other organisms

Policy information about studies involving animals; ARRIVE guidelines recommended for reporting animal research

Laboratory animals	All animal experiments were approved by the Harvard University Institutional Animal Care and Use Committee (IACUC). The following mice strains were used: wildtype (C57BL/6J, Jackson Laboratory # 000664), Mfsd2a:CreER(Q. Chen et al., 2016), BMX:CreER(Ehling et al., 2013), Myh11:CreER(Wirth et al., 2008), NG2:DsRED(Zhu et al., 2008) JAX# 008241, Ai14 (Madisen et al., 2010) JAX# 007914, Ai39(Madisen et al., 2012) JAX# 014539, Ai75(Quina et al., 2017) JAX# 014539 , ROSA26:LSL-Mfsd2a (this paper), Thy1:GCaMP6s(T.-W. Chen et al., 2013) JAX# 024275, Cav1-/- (Razani et al., 2001) JAX# 007083 , Cav1 floxed(Asterholm et al., 2012), Nos3-/- (Shesely et al., 1996) JAX# 002684 , ROSA26: PhiC31(Raymond and Soriano, 2007) JAX# 007743. Mice of both sexes were used and ages ranged from 8 to 20 weeks old.
Wild animals	The study did not involve wild animals.
Field-collected samples	The study did not involve field-collected samples.
Ethics oversight	All animal experiments were approved by the Harvard University Institutional Animal Care and Use Committee (IACUC).

Note that full information on the approval of the study protocol must also be provided in the manuscript.